

**INVESTIGATIONS OF QCD  
HADRONIZATION USING JETS  
MEASURED AT  $\sqrt{s} = 8$  TeV WITH  
THE ALICE DETECTOR.**

A Dissertation Presented for the

Doctor of Philosophy

Degree

The University of Tennessee, Knoxville

Andrew John Castro

March 2019

© by Andrew John Castro, 2019

All Rights Reserved.

# Table of Contents

<b>1</b>	<b>Introduction</b>	<b>1</b>
<b>2</b>	<b>Quantum Chromodynamics</b>	<b>4</b>
2.0.1	The QCD Lagrangian . . . . .	4
2.0.2	Scattering and Hard Processes . . . . .	5
2.0.3	Factorization . . . . .	6
2.0.4	Kinematics . . . . .	6
2.1	Jets . . . . .	7
2.1.1	Jet Finding Algorithms . . . . .	8
2.2	The Quark-Gluon Plasma . . . . .	8
2.2.1	Asymptotic Freedom and the Perfect Fluid . . . . .	8
2.2.2	Energy Loss in a Colored Medium . . . . .	9
2.2.3	The Nuclear Modification Factor . . . . .	9
2.2.4	Nuclear Collisions . . . . .	9
2.3	QGP in Proton-Proton Collisions? . . . . .	9
<b>3</b>	<b>The LHC and ALICE</b>	<b>10</b>
3.1	Overview of the LHC . . . . .	10
3.1.1	LHC Operations . . . . .	11
3.1.2	LHC Accelerator Complex . . . . .	12
3.2	The ALICE Experiment . . . . .	13
3.2.1	TZERO . . . . .	14
3.2.2	VZERO . . . . .	14

3.2.3	Inner Tracking System . . . . .	15
3.2.4	Time Projection Chamber . . . . .	16
3.2.5	Electromagnetic Calorimeter . . . . .	19
<b>4</b>	<b>The ALICE TPC Upgrade</b>	<b>23</b>
4.0.1	Physics Motivation . . . . .	23
4.0.2	Gaseous Electron Multiplier Foils . . . . .	25
4.0.3	Research and Development . . . . .	27
4.0.4	Production of the Inner Readout Chambers in the U.S. . . . .	30
4.0.5	GEM and Chamber Quality Assurance . . . . .	32
4.0.6	Outlook . . . . .	35
<b>5</b>	<b>Jet Results and Discussion</b>	<b>37</b>
5.1	Data Quality . . . . .	38
5.2	Event Selection . . . . .	38
5.3	Raw measurements . . . . .	39
5.3.1	Raw Jet Momentum Spectra in pp Collisions . . . . .	40
5.4	Unfolding . . . . .	40
5.4.1	Corrections to particle Level . . . . .	40
5.4.2	Unfolding Matrix . . . . .	40
5.4.3	Unfolded Spectra . . . . .	40
5.5	Trigger Efficiency . . . . .	40
5.6	Systematic Uncertainties . . . . .	40
5.6.1	Systematic Uncertainty to Jet Yield . . . . .	40
5.6.2	Systematic Uncertainty to Jet Energy Scale . . . . .	40
5.6.3	Total Uncertainty . . . . .	40
5.7	Corrected pp jet cross section . . . . .	40
5.7.1	Comparisons to pQCD predictions . . . . .	40
5.7.2	Jet Cross Section and Ratios . . . . .	40
<b>6</b>	<b>Conclusion and Outlook</b>	<b>41</b>

<b>Bibliography</b>	<b>42</b>
<b>Appendices</b>	<b>49</b>
A    Particle Identification via Bethe-Bloch . . . . .	50
<b>Vita</b>	<b>52</b>

# List of Figures

1.1	The fundamental particles of the Standard Model[1]. . . . .	1
2.1	Strong coupling constant ( $\alpha_s$ ) as a function of the momentum transfer (Q)[2].	5
2.2	Nuclear collision . . . . .	7
3.1	LHC accelerator complex. The four main experiments are shown in their relative locations[3]. . . . .	11
3.2	The ALICE Detector at CERN[4]. . . . .	13
3.3	ALICE tracker, multiplicity, timing, and vertex detectors located near the interaction point[4]. . . . .	13
3.4	Multiplicity measured in the V0 detector with Glauber fits corresponding to centrality[5]. . . . .	15
3.5	The ALICE Time Projection Chamber[6]. . . . .	16
3.6	The TPC readout region[7]. . . . .	17
3.7	TPC momentum and tracking resolution[8]. . . . .	18
3.8	ALICE EMCal along with super modules, tower strips, and towers[9]. . . . .	19
3.9	Energy resolution in the EMCal measured in a 2007 test beam at CERN(blue) compared to GEANT3 simulations of the EMCal(orange), fits for the parameters A, B, and C are also shown[10]. . . . .	21
3.10	Cluster Spectra from the ALICE EMCal. MinBias is shown in black while the red and blue points show the spectra using the gamma trigger at two energy thresholds[11]. . . . .	22

4.1	Simulation of the invariant mass spectra for dileptons in a typical heavy-ion run with current ALICE performance (left) and after upgrade of ALICE for Run-3 (right) in PbPb at $\sqrt{s_{NN}} = 5.5$ TeV. The dilepton yields originating from the QGP are shown (red and orange), along with background contributions from light-hadrons (blue), and charm (magenta)[12]. . . . .	25
4.2	Scanning electron microscope image of a GEM foil from top (left) and profile (right)[13]. . . . .	26
4.3	Profile of GEM with electric-field lines and gradients (left). Simulation of an ionization electron (yellow line) entering a GEM from a drift volume, amplification electrons (green dots, yellow lines) and back flow ions (red lines) are created (right)[14]. . . . .	27
4.4	ITS-TPC matching ( <i>left</i> ) and inverse momentum resolution ( <i>right</i> ) for a 4-GEM stack simulated in Garfield++ [15]. . . . .	28
4.5	Final design of the upgraded readout chambers with a stack of 4 GEMS [16].	28
4.6	dE/dx resolution of the 4-GEM IROC prototype( <i>left</i> ) and the separation power between electrons and pions as a function of gain ( <i>right</i> )[17]. . . . .	30
4.7	Energy resolution of the iron peak as measured from the prototype IROC with varying GEM voltages as a function of IBF%[17]. . . . .	30
4.8	Simulation of the four GEM (blue) layers after test beam. The configuration is such that the two GEMs closest to the drift volume, right side, absorb the amplification ions created by the two GEMs closest to the readout (right) [17].	31
4.9	Production flow of the IROCs (red), OROCs (blue), and GEM foils (green)[15]. . . . .	32
4.10	The author assembling an Inner Readout Chamber at the University of Tennessee. . . . .	32
4.11	Schematic for the setup of the GEM foil spark test ( <i>left</i> )[18] and the GEM mounted in the HV gas box ( <i>right</i> ). . . . .	33
4.12	Schematic of the gas tightness testing setup at the University of Tennessee ( <i>Courtesy of Joseph Rasson</i> ). . . . .	34

4.13	Leak rate of the 47 chambers built at Tennessee with the maximum failure rate at 0.25 ml/hr shown ( <i>Courtesy of Charles Hughes</i> ). . . . .	35
4.14	The author testing spark testing chambers next to the LHC beam line ( <i>left</i> ) and real time output from the spark test during a live beam ( <i>right</i> ). . . . .	36
1	Energy loss of a muon traversing a copper medium between 0.1 MeV to 100 TeV [1]. . . . .	50
2	Specific energy loss for the ITS( <i>left</i> ) and the TPC( <i>right</i> ) with Bethe-Bloch fits from different particle species traversing each detector[19]. . . . .	51

# Chapter 1

## Introduction

From the Vedas to the ancient Greeks, generations have described the constituents of nature in terms of indivisible ‘elements’. It wasn’t until the beginning of the 20th century that the ancient elements of earth, wind, fire, water, and the aether were abandoned for the atomic theory of nature. By the 1960’s, what would become known as the Standard Model of Particle Physics was taking shape. The five ancient elements were replaced by the fundamental particles: quarks and leptons comprising the spin 1/2 fermions and the force carrying bosons with spin 1 as seen in Fig. 1.1

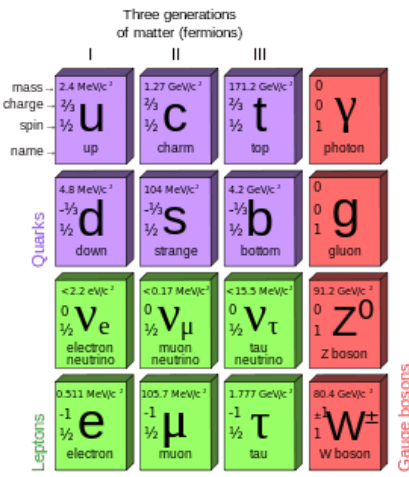


**Figure 1.1:** The fundamental particles of the Standard Model[1].

The Standard Model is the unification of the three symmetry groups,  $SU(3) \times SU(2) \times U(1)$ , representing the strong, weak, and electromagnetic forces[20]. In terms of scientific

accomplishments the Standard Model is one of the most tested theories of nature with an agreement between the theory and observed results up to ten digits[21].

Even though the Standard Model gives us a deep understanding for many natural phenomena and has a wide range of uses; understanding the evolution of the Big Bang, how atoms and molecules bond, the nature of light, to cancer treatments and nuclear security it is fundamentally an incomplete theory of nature. The fact that Gravity has yet to be unified into a quantum theory tells us that the Standard Model is incomplete. High energy experiments give us some of the most extreme conditions possible to test the Standard Model and to look for phenomena outside of the theory. Are their new symmetries and laws that manifest at high energies? Can we create dark matter or dark energy in a laboratory? Are quarks and leptons fundamental or finite in size? Do the four fundamental forces emerge from some yet unknown unified force? And why is antimatter absent in the Universe? All of these open questions are of great interest and currently form large areas of active research.

The theory of strong interactions, Quantum Chromodynamics(QCD), is described by the SU(3) group and similar in analogy to the electric charge of Quantum Electrodynamics (QED) carries color charge, red, green, and blue. Quarks and gluons are colloquially known as partons and are particles that interact via the strong force. At low energies and over large length scales partons are confined to a color neutral state and these particles must clump together into color neutral hadrons. As two colored partons began to separate, at some point it becomes energetically favorable to create a quark–antiquark pair out of the vacuum rather than expanding the distance between neighboring partons. Due to confinement, quark interactions at high energy collider experiments manifest themselves as a spray of hadrons known as a ‘jet’. The other main attribute of QCD is asymptotic freedom, as the interactions between partons becomes more energetic and the length scale decreases the strong coupling constant becomes exceedingly small,  $\alpha_{strong} \ll 1$ , and the partons freely interact with one another. Due to asymptotic freedom nuclear matter undergoes a phase transition called the Quark–Gluon Plasma (QGP) at high energies and densities

This thesis will present an overview of Quantum Chromodynamics in Chapter 2, with an emphasis on jet physics and heavy ion collisions. Chapter 3 will give a brief overview of the Large Hadron Collider and the ALICE experiment, including the relevant subsystems

for this jet analysis. Jet results from the ALICE detector along with comparissons to QCD simulations with systematic uncertainty calculations and unfolding for detector effects will be given in Chapter 4. The ALICE time projection chamber will be upgraded to a continous readout mode, the physics motivation behind this and author's contributions will be discussed in Chapter 5. Chapter 6 will serve as a final discussion, outlook, and conclusion.

# Chapter 2

## Quantum Chromodynamics

In 1968 deep inelastic scatterings performed at the Stanford Linear Accelerator Center showed that the proton had internal structure[22] called partons at the time. Within a decade of this discovery the partons were broken into two categories: the mass carrying fermions were known as the quarks and the gauge boson force carriers were called gluons. The interactions of these two types of particles were described by the quantum field theory known as quantum chromodynamics (QCD) and by the SU(3) symmetry group. SU(3) guarantees that color charge is conserved and this results in quarks grouping together into ‘colorless’ hadrons.

### 2.0.1 The QCD Lagrangian

QCD is the strongest of the known fundamental forces. It is a gauge field theory described by the Lagrangian density

$$\mathcal{L} = -\frac{1}{4}F_{\mu\nu}^\alpha F_\alpha^{\mu\nu} - \alpha_s(\bar{q}_j \gamma^\mu T_\alpha q_j)G_\alpha^\mu + \bar{q}_j(i\gamma^\mu \partial_\mu - m)q_j \quad (2.1)$$

where  $q$  and  $\bar{q}$  represent the color anti-color fields summed over color  $j$ ,  $\alpha_s$  is the strong coupling strength,  $\gamma^\mu$  is the Dirac gamma matrix,  $G_\alpha^\mu$  is the gauge field for color  $\alpha$ , is similar in analogy to the  $\mathbf{W}$  matrix from the electroweak theory.  $F_{\mu\nu}^\alpha$  is the field strength tensor and it describes the gluon interactions. The first term of the Lagrangian is the gluon contribution and carries no mass term. The second term of the Lagrangian describes how quarks and

gluons interact with each other. The final term describes quark interactions and the coupling between them and will be explored further in this thesis.

At short distances, less than  $0.2 \text{ fm}$ , the strong coupling constant becomes exceedingly small and second term of the Lagrangian displays an important property known as asymptotic freedom[23].

$$\alpha_s = \frac{1}{\beta_0 \ln(Q^2/\Lambda^2)} \quad (2.2)$$

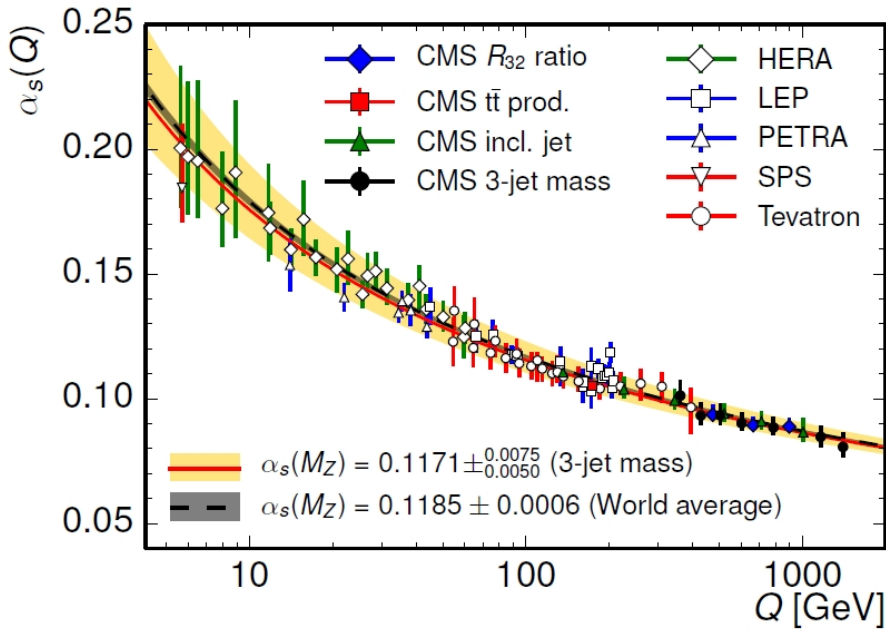


**Figure 2.1:** Strong coupling constant ( $\alpha_s$ ) as a function of the momentum transfer ( $Q$ )[2].

### 2.0.2 Scattering and Hard Processes

One of the best places to fundamentally test QCD is with high energy hadron colliders such as those found at CERN, Fermilab, and BNL<sup>1</sup>. Hard probes, partons that interact with a high momentum transfer (large  $Q^2$  and all  $\alpha_s$ ), can be probed using perturbation theory. The time scale that a hard probe is created in a high energy collision is on the order of  $\tau \approx 1/p_T \approx 0.1 \text{ fm}/c$  which probes the initial state these interactions. As these partons separate from one another

---

<sup>1</sup>Discussed in detail in Chapter 3

$$d\sigma^{pp \rightarrow jet} \sim f_{a/A}(x_1, Q^2) \otimes f_{b/B}(x_2, Q^2) \otimes d\sigma_{ab \rightarrow c+X}(x_1, x_2) \otimes D_{c \rightarrow h/jet}(z, \mu^2) \quad (2.3)$$

### 2.0.3 Factorization

#### Hadronization

#### Partonic Distribution

### 2.0.4 Kinematics

; Before I give a detailed discussion of the physics and observables in high energy and nuclear physics it would be advantageous to define some terms and go over a few formulas.

In a circular particle accelerator a beam of relativistic particles travels along a beamline. The coordinates along this beamline are broken into longitudinal and transverse component. The momentum can similarly be described in these coordinates as the longitudinal and transverse momentum, denoted as  $\mathbf{p}_L$  and  $\mathbf{p}_T$ . For cylindrical detectors like ALICE<sup>2</sup> it is more advantageous to use a cylindrical coordinate system of with  $\theta$  as the polar angle and  $\phi$  as the azimuth angle. Relativistic particles traveling along the beamline will have

$$y = \frac{1}{2} \ln \frac{E + |\mathbf{p}|}{E - |\mathbf{p}|} \quad (2.4)$$

$$\eta = \frac{1}{2} \ln \frac{|\mathbf{p}| + p_L}{|\mathbf{p}| - p_L} \quad (2.5)$$

Therefore in terms of cartesian coordinates with the x-y plane as the plane transverse to the beamline and the z component as the component along the beam line we can derive the following relationships

$$p_x = p_T \cos \phi \quad (2.6)$$

$$p_y = p_T \sin \phi \quad (2.7)$$

---

<sup>2</sup>See Chapter 3

$$p_z = p_T \sinh \eta \quad (2.8)$$

The advantage of using the azimuthal angle and pseudorapidity over cylindrical or Cartesian coordinates is that given any two particles, the separation between  $R = \sqrt{(\phi_i - \phi_j)^2 + (\eta_i - \eta_j)^2}$  is invariant under all Lorentz boosts along the beamline.

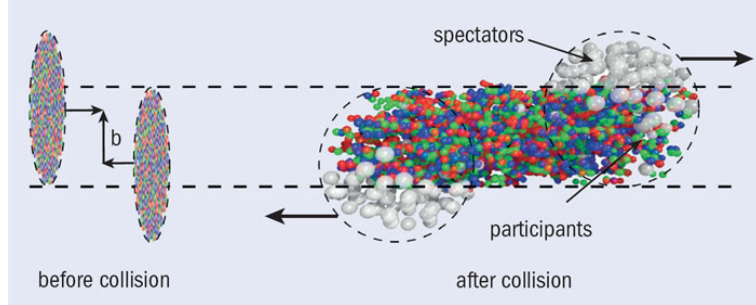


**Figure 2.2:** Nuclear collision .

In nuclear collisions the offset between the centers of two nuclei is known as the impact parameter ( $b$ ) as seen in Figure 2.2. Measuring the impact parameter in an experimental setting is non-trivial and model-dependent. The distribution of nucleons in the nucleus is modeled after a Glauber distribution[24]. The Glauber model predicts that there is a direct correlation between the impact parameter of a nuclear collision and to the inelastic differential cross section ( $\sigma_{inel}$ )[25].

$$c(b) = \frac{\int_0^b \frac{d\sigma}{db} db}{\int_0^\infty \frac{d\sigma}{db} db} = \frac{1}{\sigma_{inel}} \int_0^b \frac{d\sigma}{db} db \quad (2.9)$$

## 2.1 Jets

Hard probes (large  $Q^2$  interactions), are produced in the earliest stages of a high energy collision during the largest momentum transfer. As two highly energetic partons propagate away from one another they will instigate a shower of daughter partons via gluon radiation and the generation of  $q\bar{q}$  pairs. The clustering of these daughter partons or the final state hadrons they form into is colloquially known as a ‘jet’. Jets have been the workhorse for probing QCD phenomena by both theoretically and experimentally for over 30 years.

### 2.1.1 Jet Finding Algorithms

Although, it may simple to have a conceptual grasp of what a jet ‘is’ there is no unambiguous definition, both experimentally and theoretically, for how to define a jet. This is due to the fragmentation process by which partons form into their final state hadrons is not calculable pertubatively. The earliest jet measurements used multiple definitions which complicated comparisons between experiments and theoretical calculations. In 1990, the Snowmass Accord[26] was held in order to standardized the definition of a jet between experimentalists and theoretcians. The agreement maintained that any algorithm that clusters particles into a jet must be both infrared and collinear safe (IRC). If a high-momentum parton radiates a soft gluon this emission should not affect the

Although there are a number of jet finding algorithms available, I will only focus on algorithms that are both collinear and infrared safe.

## 2.2 The Quark-Gluon Plasma

### 2.2.1 Asymptotic Freedom and the Perfect Fluid

#### Hydrodynamics

The conservation laws for a relativistic fluid conserve the charge current and energy-momentum tensor of the expanding fluid such that:

$$\partial_\mu N_i^\mu = 0 \tag{2.10}$$

$$\partial_\mu T^{\mu\nu} = 0 \tag{2.11}$$

## 2.2.2 Energy Loss in a Colored Medium

## 2.2.3 The Nuclear Modification Factor

## 2.2.4 Nuclear Collisions

# 2.3 QGP in Proton-Proton Collisions?

As previously stated a QGP is believed to be absent in proton-proton collisions, thus any signature of a QGP should likewise be absent. One way of quantifying the presence of the QGP is via the Bjorken energy density.

$$\varepsilon = \frac{1}{\tau A} \frac{dE_T}{d\eta} \quad (2.12)$$

where  $A$  is the transverse area of the nuclei,  $\tau$  is the proper time, and  $dE_T/d\eta$  is the transverse energy per unit pseudorapidity. It can be shown that the 150 MeV critical temperature need for the phase transition to the QGP corresponds to  $1 - 3 \text{GeV}/fm^3$  energy density. The quantity  $dE_T/d\eta$  can be related to the mean transverse momentum  $\langle p_T \rangle$  and particle multiplicity<sup>3</sup> per unity pseudorapidity as:

$$\frac{dE_t}{d\eta} \approx \langle p_T \rangle \frac{dN}{d\eta} \quad (2.13)$$

where  $\langle p_T \rangle$  is the mean transverse momentum and  $dN/d\eta$  is the particle multiplicity per unit pseudorapidity. This suggest that in very high multiplicity proton-proton events signatures of the QGP may be present. This is one of the most active and newest areas of research in heavy ion physics.

---

<sup>3</sup>Multiplicity is defined as the number of particles per event

# Chapter 3

## The LHC and ALICE

### 3.1 Overview of the LHC

The Large Hadron Collider (LHC)[27] is a circular particle accelerator located on the Franco-Swiss border near the city of Geneva. It is operated by the European Organization for Nuclear Research (CERN) and has carried out proton-proton (pp), lead-proton (pPb), and lead-lead (PbPb) collisions at center of mass energies of 0.9-14 TeV, 5.0 TeV, and 2.76-5.5 TeV, respectively. The LHC is approximately 17 miles in circumference and located 200 meters underground. It is located inside the old accelerator tunnel used by the Large Electron-Positron[28] collider of the 1980's. There are over 8000 physicists and engineers making up the four main experiments at the LHC: ATLAS[29], CMS[30], LHCb[31], and ALICE[32]. Numerous physics results have been published, with the most famous being the discovery of the Higgs boson in 2012[33][34].

Figure 3.1 shows a schematic of the LHC along with the pre-accelerators that help to accelerate protons and ions to their final energies before a collision at one of the four experimental interaction points(IP). Protons are injected into the LHC together in groups called ‘bunches’. Every bunch is comprised of about 120 billion protons with about 50 nanoseconds between the arrival of the next bunch. The bunch scheme during the heavy-ion run is reduced to 200 nanoseconds due to the high multiplicity of the events and additional computational resources needed.

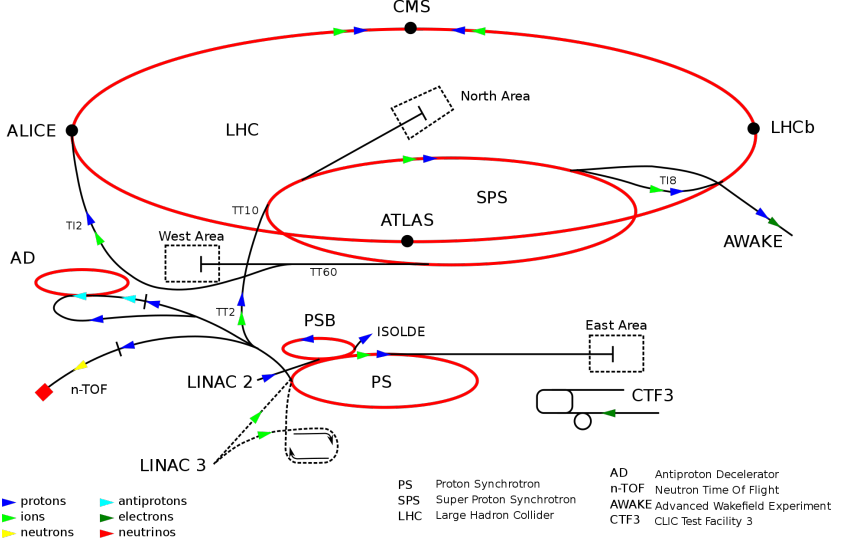


**Figure 3.1:** LHC accelerator complex. The four main experiments are shown in their relative locations[3].

### 3.1.1 LHC Operations

The LHC first attempted particle collisions in September of 2008. The initial ramping up of the super conducting magnets led to mechanical failure of the helium pipes inside of the LHC beam line. This fault caused the LHC to remain shut down for over a year while the accelerator was repaired and new safety procedures were implemented. The first successful collisions occurred in 2009 with proton collisions at a reduced energy of 0.9 TeV. 2010 marked the beginning of a new era in the high energy frontier with proton collisions at a record setting 7 TeV. The only other major fault that has occurred was in the summer of 2016. A stone marten chewed through a high voltage line in a power transformer on a ground level building at the LHC. The LHC went offline for about a week while repairs occurred and quickly resumed the physics program. Unfortunately, the marten did not survive.

The typical operating year at the LHC allows for any repairs or upgrades on any of the experiments to be performed during the offline period for the first few months. After the offline period the proton physics program begins and lasts until approximately mid-November. The heavy ion program lasts until the first week of December, after which the LHC shuts down for the remainder of the year. From 2014 until early 2015 the LHC was

shutdown for major renovations and upgrades to the accelerator and a number of sub-detectors on each experiment,. This was known as long shutdown 1 (LS1). After 2018, the LHC will go through another shutdown (LS2) during which the accelerator will have a high luminosity (Hi-Lumi) upgrade. This will be discussed in detail along with the upgrades that will be done to ALICE in chapter 4.

### 3.1.2 LHC Accelerator Complex

The LHC accelerator complex is a succession of particle accelerators that increase the energy of particles before they are injected into the next accelerator. Hydrogen atoms are first passed through a high voltage environment that strips any electrons around the nuclei. Once the nuclei are stripped of their electrons they are injected into the linear accelerator(LINAC). The LINAC uses radio frequency cavities to accelerate particles to 50 MeV before they enter the first circular accelerator the Proton Synchrotron(PS). The PS begins to focus the protons into bunches and further accelerates them to 1.4 GeV before the beam enters the Super Proton Synchrotron(SPS). The SPS will further accelerate the particles to 450 GeV. The beam is then injected into the LHC. Once the beams are injected into the LHC they are accelerated to the final collision energy. Afterwards the beams get ‘squeezed’, or tightly focused, with a series of quadrupole magnets. The final step is to ‘adjust’ the two beams to overlap with one another at each experiments IP. Once the adjust phase is completed, collisions will occur at each experiment and data begins to get collected. This entire process from stripping the electrons to having collisions in each IP takes 20 minutes.

In order for the beam parameters to be maintained in the LHC, numerous dipole and quadrupole magnets are deployed to accelerate, focus, and bend the particle beams. The magnets use a superconducting niobium-titanium alloy that are maintained at an operating temperature of 1.9 K using helium-4. Upgrading these magnets is one of the major goals during LS2 as part of the Hi-Lumi upgrade of the LHC[35].

## 3.2 The ALICE Experiment

A Large Ion Collider Experiment(ALICE) is a general purpose detector that covers a solid angle of  $4\pi$  around the IP. It is 26 m long, 16 m high, 16 m wide, and weighs approximately 10,000 tons[35]. Like many other large scale detectors ALICE is made up of a number of sub-detectors<sup>1</sup> that perform tracking, particle identification(PID), timing, vertex reconstruction, and calorimetry.

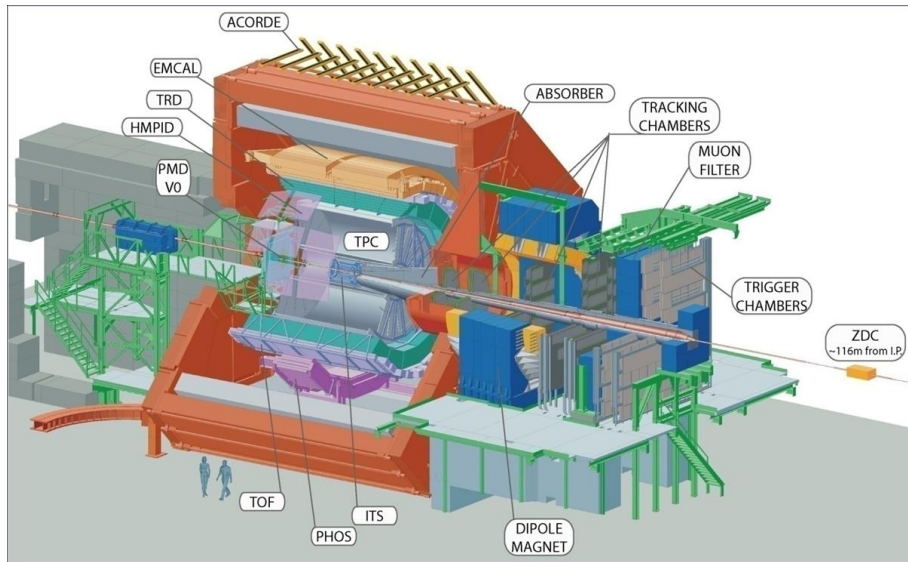


**Figure 3.2:** The ALICE Detector at CERN[4].

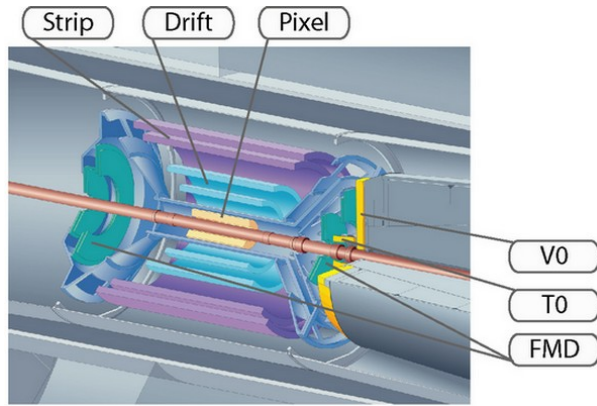


**Figure 3.3:** ALICE tracker, multiplicity, timing, and vertex detectors located near the interaction point[4].

---

<sup>1</sup>In total ALICE has 18 sub-detectors

Figure 3.2 shows the ALICE detector with human figures to set the scale. Figure 3.3 shows the area closest to the IP with the TZERO, VZERO, Inner Tracking System and Forward Multiplicity Detector; these detectors give basic information on the collision such as vertex location, centrality, timing. Further out from the central region are a number of tracking detectors like the Time Projection Chamber and Time-of-Flight detectors that focus on measuring charged particle momentum and PID. Next are the calorimeters that measure particle and jet energies, such as the Electromagnetic Calorimeter, Photon Spectrometer, and the Dijet Calorimeter. All of these sub-detectors are housed in the L3 magnet seen as the red octagon in Figure 3.2. The L3 magnet provides a uniform magnetic field over the central area of ALICE and is responsible for the high PID performance ALICE has over a wide kinematic region[36]. At high rapidity, there is a muon tracker and trigger for muon identification. The following sections give a more detailed discussion of the sub-detectors used for this analysis

### 3.2.1 TZERO

The TZERO(T0)[37] detector is a double layer Cherenkov counter located at 70 cm(T0A) and 370 cm(T0B) from the IP. T0 functions as a trigger and timing detector that determines the precise moment in time at which an event ‘starts’ in the ALICE detector. The timing information from the T0 is fed to other sub-detectors, like the Time-of-Flight and Time Projection Chamber detector, for track reconstruction. The T0 also gives feedback on the target luminosity of the ALICE experiment to the LHC operations center.

### 3.2.2 VZERO

The VZERO(V0)[38] detector is a double layer scintillator array and similar to the T0 is asymmetrically placed at a distance of 86 cm(V0A) and 329 cm(V0C) away from the primary IP. It provides the ‘minimum bias’(MinBias)<sup>2</sup> trigger information for events and centrality information during the heavy-ion run. Centrality<sup>3</sup> is determined by measuring the

---

<sup>2</sup>A MinBias event is unsurprisingly defined as an event with the least amount of bias possible. Events recorded with a MinBias trigger attempt to not artificially prefer either diffractive or non-diffractive processes over one another[39].

<sup>3</sup>See Section 2.0.4

multiplicity amplitude from the V0 and fitting these results to a Glauber<sup>4</sup> distribution, as seen in Figure 3.4. The V0 is also capable of precision measurements of the target luminosity in the ALICE detector.

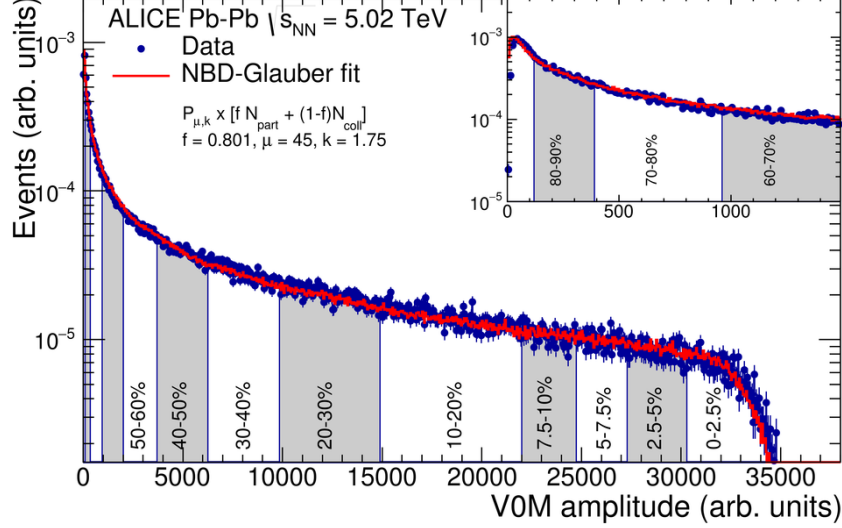


**Figure 3.4:** Multiplicity measured in the V0 detector with Glauber fits corresponding to centrality[5].

### 3.2.3 Inner Tracking System

The Inner Tracking System(ITS)[40] is six layers of solid state silicon detectors. Closest to the beam line are two layers of Silicon Pixel Detectors. The next two layers are Silicon Drift Detectors and furthest from the beam line are two layers of Silicon Strip Detectors. The main purpose of the ITS is to perform momentum measurements, PID, and vertex reconstruction of charged tracks. PID<sup>5</sup> is performed by measuring the ionization energy,  $\frac{dE}{dx}$ , of charged particles as they traverse the detector[41]. The ITS has a spatial resolution of  $100 \mu\text{m}$ . This allows for measurements of short lived hadrons by reconstructing secondary vertices, which is the distance of closest approach a track has to the primary vertex.

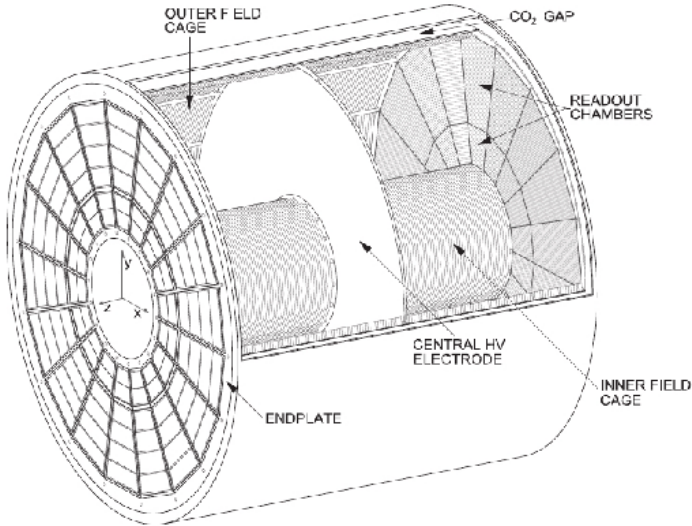


**Figure 3.5:** The ALICE Time Projection Chamber[6].

### 3.2.4 Time Projection Chamber

The Time Projection Chamber(TPC)[6] is a gaseous charged particle tracker and the largest of its kind in the world. The TPC has full azimuthal coverage, a pseudorapidity acceptance of  $|\eta| \leq 0.7$ , and a volume of  $93 m^3$ . Figure 3.5 shows a schematic of the TPC. As charged particles traverse the drift volume of the TPC, they ionize the gas inside<sup>6</sup>. A central cathode in the TPC with a voltage of 100 kV induces a uniform electric field of 400 V/m along the beam axis throughout the drift volume. Ionized electrons will drift down to the cylindrical endcaps of the TPC where the read-out chambers(ROC) are located. There are 18 ROCs on each side of the TPC which are further broken into a Inner Read Out Chamber(IROC) and Outer Read Out Chamber(OROC).

#### The TPC readout

The TPC incorporates a Multi-Wire Proportional Chamber(MWPC) design for amplification and copper pads for readout<sup>7</sup>. Ionized electrons created from charged particles take approximately  $100 \mu s$  to move from the drift volume to the readout region. Once these

---

<sup>4</sup>A Glauber model treats the nucleons composing a nucleus as hard shells, more can be found here [24].

<sup>5</sup>See Appendix A

<sup>6</sup>The TPC has operated with  $Ne - CO_2$  (90-10) and  $Ar - CO_2$  (90-10) gas mixtures in the past

<sup>7</sup>Their are 72 MWPCs and 500K copper pads in the ALICE TPC

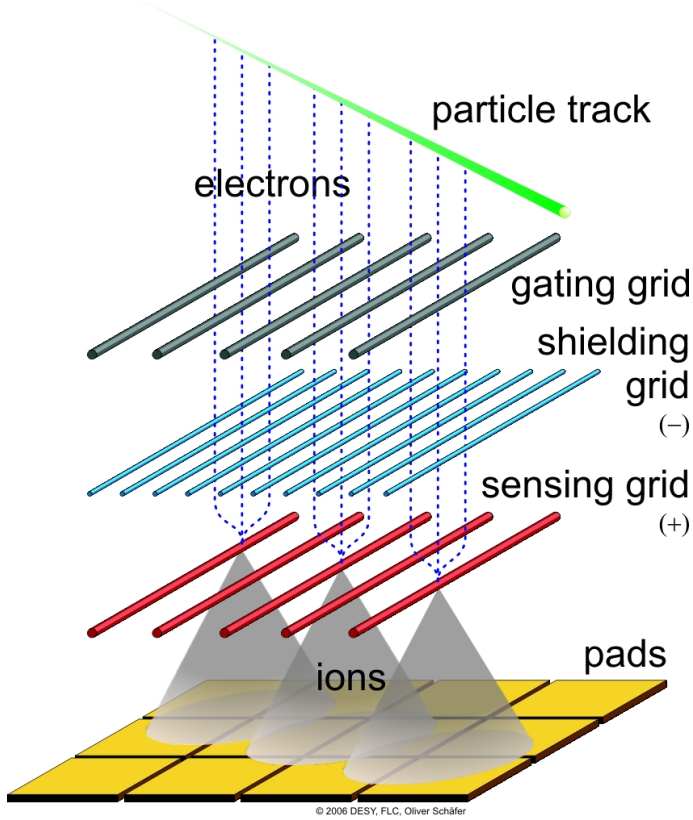


**Figure 3.6:** The TPC readout region[7].

electrons enter the readout region they will undergo an amplification process with the MWPC, seen as the sensing grid wires in Figure 3.6. This amplification process will turn the few dozen ionization electrons generated from a charged particle into thousands of amplification electrons that are easily sensed by the cooper pads and read from the front-end electronics(FEE). Amplification using MWPCs has the disadvantage of creating thousands of ions known as ‘backflow ions’ that can move back into the drift volume of the TPC. The presence of backflow ions in the drift volume of the TPC will cause distortions in the uniform electric field of the TPC. These distortions are known as ‘space-charge’ distortions and will compromise the physics performance of the TPC. In order to minimize the space-charge distortions the TPC incorporates a gating grid[? ]. Once an event is detected in the readout electronics of the TPC a high voltage is induced on the gating grid. This will capture any backflow ions moving from the amplification region to the drift volume. When engaged the gating grid introduces a dead time as any ionization electrons from new events occurring in ALICE will also get captured. The current configuration of the gating grid is

designed to engage it for 300  $\mu\text{s}$  after an event is first detected. This has been shown to absorb approximately 99% of the backflow ions created while preserving the TPC physics performance. The deadtime due to the gating grid along with the drift time for charged particles in the TPC limits the readout to 3.5 kHz. Upgrading the triggered operation of the current TPC to a continuous readout for the Hi-Lumi upgrade of the LHC will be discussed in detail in Chapter 4.

## TPC Performance

In order to reconstruct the trajectory of a particle, an iterative process known as the Kalman filter approach is deployed. The x-y coordinate which is perpendicular to the beamline are determined via the signal induced on the copper pads. The z component which is parallel to the beamline is reconstructed using the timing information from the T0.

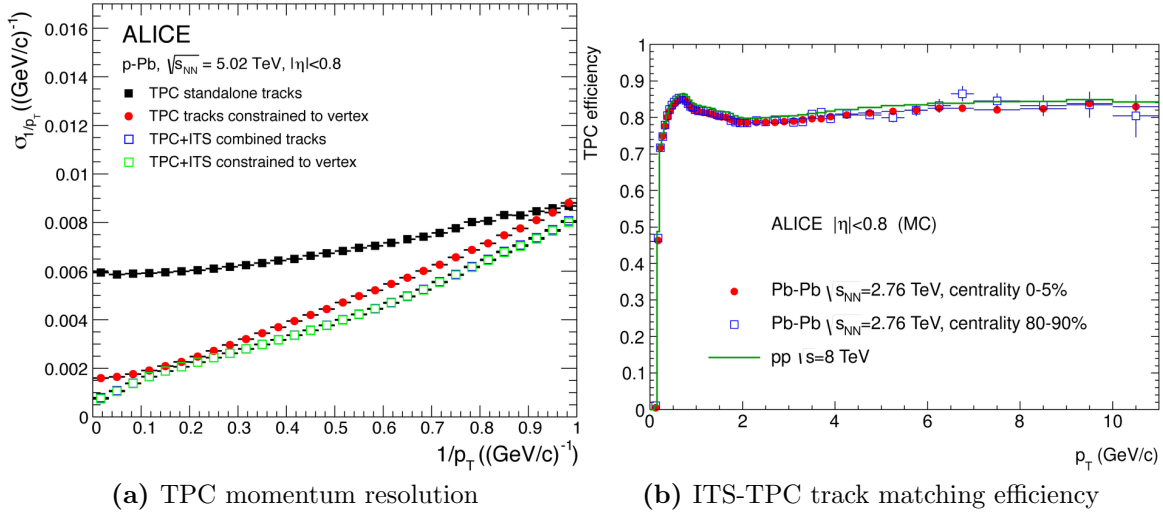


**Figure 3.7:** TPC momentum and tracking resolution[8].

The TPC has excellent momentum resolution between 150 MeV/ $c$  to 100 GeV/ $c$ [42]. Figure 3.7a shows the inverse momentum resolution as being below 10% in black. The momentum resolution was further improved to almost 5% over the full kinematic range by matching TPC tracks to ITS tracks and constraining those tracks to originate from the primary vertex region, red and green respectively. The matching efficiency between ITS tracks to TPC tracks is stable at about 80%, Figure 3.7b.

### 3.2.5 Electromagnetic Calorimeter

The Electromagnetic Calorimeter(EMCal)[43] is a lead based sampling calorimeter located at a radius of 4.5 meters from the beam pipe. It covers a pseudorapidity of  $|\eta| \leq 0.7$  and has azimuthal coverage of  $\Delta\phi = 107$  deg.

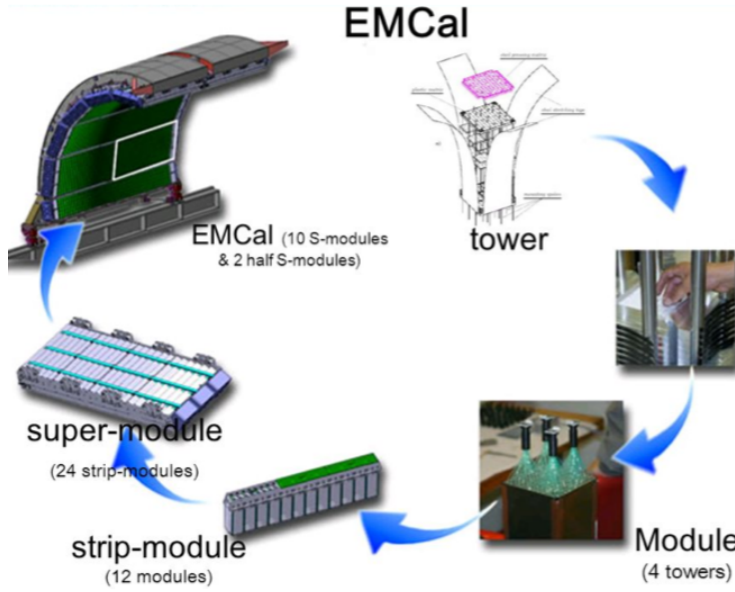


**Figure 3.8:** ALICE EMCal along with super modules, tower strips, and towers[9].

Figure 3.8 shows the layout of the EMCal. The smallest element of the EMCal is the ‘tower’<sup>8</sup>. The tower serves as the readout and is made up of several layers of alternating scintillator and Pb-absorber. Particles that interact via the electromagnetic force initiate a shower in the absorber material in the tower. This electromagnetic shower induces light in the scintillator to accumulate in the avalanche photodiodes(APD) in proportion to the particle’s energy. A ‘module’ is an array of four towers that share readout electronics. Twelve modules will be placed in a single strip that provides support to the structure. The largest component of the EMCal is the super-module, consisting of 1,100 towers, which serves as the mounting structure to the ALICE detector. In 2015 Dijet Calorimeter(DCAL) was installed in the ALICE detector to perform back-to-back jet measurements.

---

<sup>8</sup>There are 12K towers in the EMCal

## EMCal Performance

As particles enter the EMCal they initiate an electromagnetic shower. The shower of electromagnetic particles spans several neighboring towers, these towers are grouped together into ‘clusters’ and the Analog-To-Digital Conversion(ADC) signal from the clusters corresponds to the energy deposited by the particle. The EMCal was designed so that photons and electrons will fully shower inside of the tower region and thus fully deposit their energy. Hadrons on the other hand will punch through the EMCal and only deposit a small fraction of their energy. PID can be performed using the EMCal via track-cluster matching from the TPC. TPC tracks are geometrically matched to the centroid of a cluster and if no track is matched the cluster originated from a photon. If a track is matched, then the ratio of E/P, the energy of a matched cluster to the momentum of a TPC track, can be used to separate electrons from hadrons.

The energy resolution of the EMCal follows the form seen in equation 3.1

$$\frac{\sigma}{E} = \sqrt{A^2 + \frac{B^2}{E} + \frac{C^2}{E^2}} \quad (3.1)$$

where E is the cluster energy, A characterizes stochastic fluctuations such as photon collection efficiency, B is a function of the systematic effects such as detector non-uniformity, and C is a function of the noise in the Front-end electronics.

As seen in figure 3.1 excellent agreement exists between the measured performance of the EMCal compared to simulations in a kinematic range between  $10\text{GeV} - 100\text{GeV}$ . The stochastic term, A, is the largest source of uncertainty in the energy resolution due to the EMCal being a sampling calorimeter. Unlike the TPC the resolution improves at high- $p_t$  making the EMCal ideal for measuring high energy particles and jets

## EMCal Trigger

Due to the high luminosity in the LHC only a small fraction of events may be recorded to disk for later analysis. ALICE employs a variety of triggers to record events that have the highest value for performing quality physics analysis. The EMCal can trigger on events in order to increase the effective sample size for high- $p_T$  jets, photons, and electrons. The

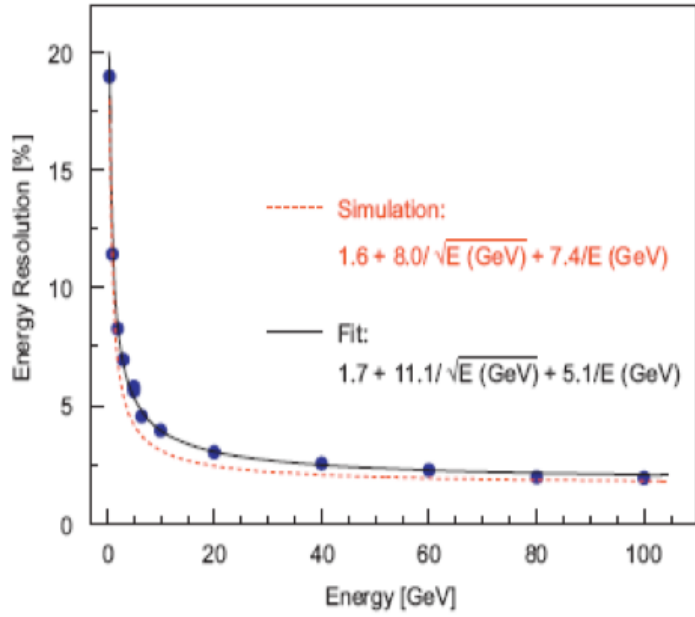


**Figure 3.9:** Energy resolution in the EMCal measured in a 2007 test beam at CERN(blue) compared to GEANT3 simulations of the EMCal(orange), fits for the parameters A, B, and C are also shown[10].

two main triggers[44][45] for the EMCal are a jet trigger and a gamma trigger. The gamma trigger is comprised of a 4x4 patch of EMCal towers, while the jet trigger is a 16x16 patch of towers. Once the gamma trigger has surpassed a minimum energy threshold of 5 GeV[46] the event is tagged as a gamma event and the patch location is recorded.

EMCal jet triggered events have an energy threshold of 20 GeV and are similarly tagged and recorded. Figure 3.10 shows the spectra from clusters measured in the EMCal using MinBias data in black and the gamma trigger from the EMCal set to two thresholds, 5 GeV and 7 GeV. Recording the events that satisfy the EMCal triggers introduces a bias towards high- $p_T$  processes, however by using events that had an EMCal trigger we can extend the kinematic range of an inclusive jet measurement as seen in Figure 3.10. In order to account for this bias it is necessary to calculate a trigger efficiency by comparing spectra from inclusive jets recorded using the MinBias trigger to the spectra generated from the EMCal triggers. The calculation of the trigger efficiency will be discussed in depth in section ??

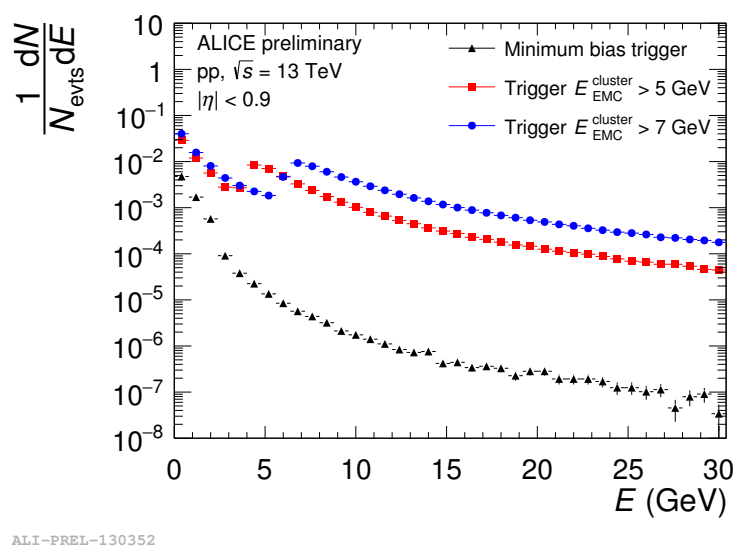


**Figure 3.10:** Cluster Spectra from the ALICE EMCal. MinBias is shown in black while the red and blue points show the spectra using the gamma trigger at two energy thresholds[11].

# Chapter 4

## The ALICE TPC Upgrade

From 2014 until 2018, I worked on the upgrade of the TPC to a continuous readout. This includes working on a test beam in 2014 for a prototype Read-Out Chamber (ROCs) using Micropattern Gaseous Detectors (MPGD) over the current Multi-Wire Proportional Chamber (MWPC) design. Once a final design for the new ROCs was chosen the production of the new Inner Read-Out Chambers (IROCs) using a stack of four Gaseous Electron Multiplier (GEM) foils took place at the University of Tennessee. During this period I assembled 49 new IROCs. In 2018, I traveled to Yale University and CERN to help with quality assurance of the IROCs built at Tennessee.

### 4.0.1 Physics Motivation

After the 2018 heavy-ion run ends, the LHC will begin the second long shutdown (LS2) and upgrade to the High Luminosity LHC (Hi-Lumi LHC)[47] which was briefly mentioned in section 3.1. The goal of the LHC upgrade is to move into an era of high precision measurements of rare QCD processes and increase the production of soft probes. Once the upgrade is complete the expected event rate in ALICE will be 50 kHz in MinBias PbPb collisions. This will lead to a factor of x100 increase in MinBias data and a factor of x10 increase in high- $p_T$  triggered data recorded by ALICE.

The ALICE experiment has focused on probing the thermodynamic properties of the QGP in the past. The increase in event rate expected from the Hi-Lumi LHC would open new ways to probe the QGP including[12]:

- Increasing the production of jets and allowing separation of jet measurements based on the flavor of the initial parton.
- Studying the production mechanisms of light-nuclei, antihyper-nuclei, and other exotic hadrons.
- Probing the initial state temperature and equation of state of the QGP by measuring low-mass dileptons that originate from the earliest stages of a heavy-ion collision.
- Increase the yields of heavy-flavor mesons reconstructed via the secondary-vertices.

In order to do this ALICE will implement a number of upgrades [48] during the shutdown that include:

- Replacing the V0 and T0 detectors with a combined detector, called the Forward Interaction Trigger (FIT)[49].
- Improving the ITS and Muon Tracker spatial resolution by using Monolithic Active Pixel Sensors (MAPS)[50][51].
- Removing the 400 nanosecond dead time associated with the TPC and upgrade the FEE cards to handle the increase in data bandwidth[12].
- New Online/Offline ( $O^2$ ) data processing architecture[52].

Leptons weakly couple to the QGP[53] and by studying these the initial states in heavy ion collisions may be probed[54]. Figure 4.1 shows a simulation of the mass spectra for dileptons between  $0 \text{ GeV}/c - 1 \text{ GeV}/c$  using the current ALICE central detectors with tight kinematic cuts (left). The yields that are quantifiable do not allow for the separation of leptons originating from the QGP from those originating from background sources. After the increase in event rate and the upgraded ITS with improved tracking capabilities, measuring

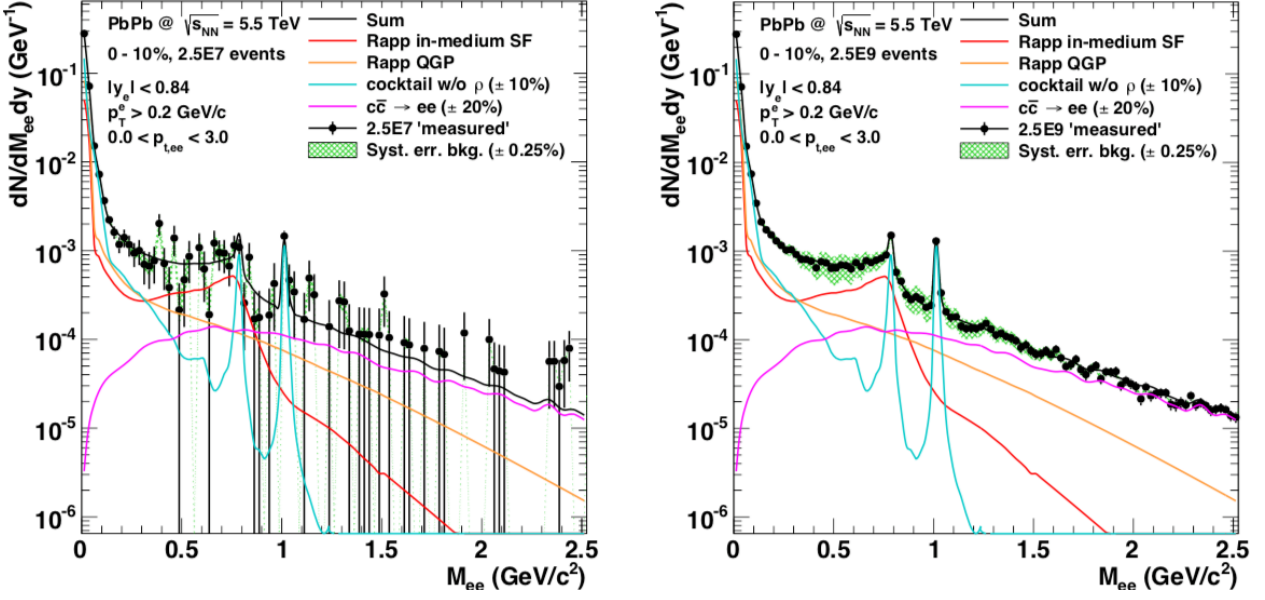


**Figure 4.1:** Simulation of the invariant mass spectra for dileptons in a typical heavy-ion run with current ALICE performance (left) and after upgrade of ALICE for Run-3 (right) in PbPb at  $\sqrt{s_{NN}} = 5.5$  TeV. The dilepton yields originating from the QGP are shown (red and orange), along with background contributions from light-hadrons (blue), and charm (magenta)[12].

the low-mass dileptons that interacted with the QGP will be possible as shown on the right of Figure 4.1.

The TPC used in the ALICE experiment along with the readout was discussed in section 3.2.4. The ALICE collaboration first proposed an upgrade of the TPC in 2012 with a Letter of Intent (LoI)[12]. A Technical Design Report(TDR)[16] was published in 2013 with an initial design overview. An addendum to the TDR[17] was published in 2015 after the performance of prototype ROCs was measured on a test beam at CERN in 2014. The overall goals of the TPC upgrade are to continuously readout events in the high luminosity environment expected after LS2, to minimize the accumulation of space-charge distortions in the drift field, and to maintain the PID and tracking performance of the current TPC.

#### 4.0.2 Gaseous Electron Multiplier Foils

Gaseous Electron Multiplier (GEM) Foils were first proposed by CERN physicist Fabio Sauli in 1997[55]. GEMs belong to a new form of detector technology known as Micropattern

Gaseous Detectors[56] that use microelectronic or chemical etching techniques to print a readout structure onto a material surface.

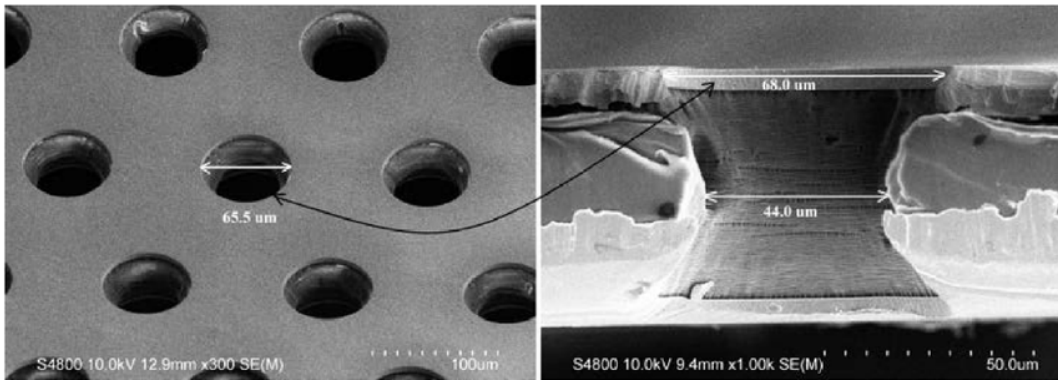


**Figure 4.2:** Scanning electron microscope image of a GEM foil from top (left) and profile (right)[13].

GEM foils are a Kapton sheet, typically  $50 \mu m$  thick, with a thin copper coat on both sides of the surface. A weak acid and stencil are used to chemically etch holes throughout the foil. Typically, the holes are between  $10 \mu m$  -  $100 \mu m$  in diameter and between  $100 \mu m$  -  $300 \mu m$  in pitch as seen in Figure 4.2. A few hundred volts is applied to each of the copper surfaces of the GEM foil causing a strong electric field to be induced in the GEM holes<sup>1</sup>.

When a ionization electron from a charged track enters a GEM hole it will cause an avalanche of electrons and ions to be produced, amplifying the signal, to MWPCs. Due to the high voltage and strong electric fields around the GEM foil, any back flow ions created from the avalanche will get absorbed by the copper surfaces on the GEM foil, as seen in Figure 4.3.

The configuration of the pitch and size holes on a GEM foil is directly correlated to the amplification properties and ability to capture back flow ions. GEMS with larger holes or shorter pitch between the holes will have more amplification but will also be more ineffective at capturing ions. Likewise, GEMs with shorter holes or larger pitch will have better ion capture abilities yet worse amplification properties. By stacking multiple GEMs on top of one another it is possible to maximize the amplification properties and minimize the backflow.

Creating GEMs with a uniform hole distribution and stacking them in a consistent manner in order to minimize the overlap of holes from one layer to another restricted

---

<sup>1</sup>The electric field is on the order of  $10 \text{ kV/cm}$

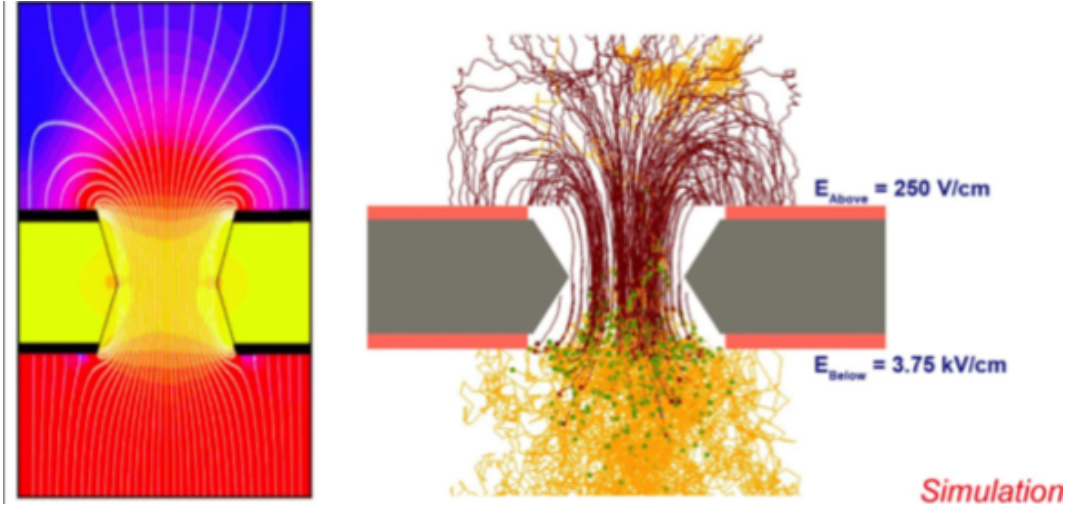


**Figure 4.3:** Profile of GEM with electric-field lines and gradients (left). Simulation of an ionization electron (yellow line) entering a GEM from a drift volume, amplification electrons (green dots, yellow lines) and back flow ions (red lines) are created (right)[14].

them to small prototypes and impeded their use on large experiments. Around 2010 two methods were developed, the single-mask technique[57] and the NS2 assembly[58], which allowed for a systematic way of etching holes and stretching GEMs so they could be properly aligned. These methods allowed for GEMs to become a viable amplification device for large experiments. As of 2018 the TOTEM, COMPASS, ATLAS, and LHCb experiments have all incorporated GEMs in their trackers. Future colliders, such as the Electron-Ion Collider (EIC), plan on using them[59].

#### 4.0.3 Research and Development

Initially, it was decided that the new ROCs would incorporate a stack of three GEMs with a hole geometry similar to the one incorporated on the LHCb experiments[60] tracking detector. This was a starting point to bench mark performance for the ALICE TPC upgrade as well as an opportunity to use experts in GEM technology already present at CERN. The first phase of the R&D involved simulating the performance of the LHCb 3-GEM stack in the high event rate environment expected after the Hi-Lumi LHC upgrade using a the software package called Garfield++[? ], which is a GEANT4[61] add-on package built to simulate MPGDs. It was quickly observed from the simulations that a 3-GEM stack would

be insufficient in maintaining the performance needed for the TPC while minimizing the ion back flow. An additional layer of GEM was added to the 3-GEM stack in simulation and it was observed that this configuration would preserve the TPC performance.

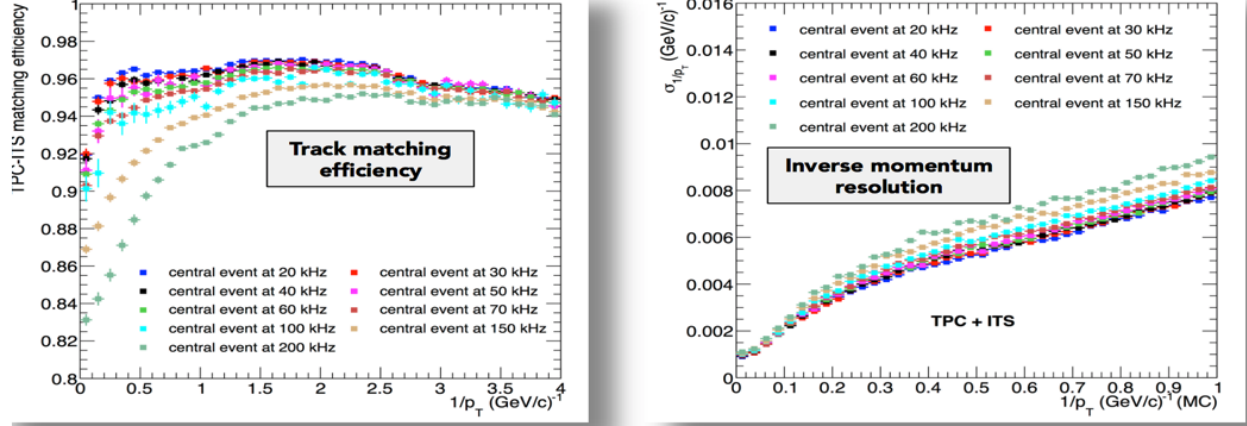


**Figure 4.4:** ITS-TPC matching (*left*) and inverse momentum resolution (*right*) for a 4-GEM stack simulated in Garfield++ [15].

Figure 4.4 shows simulations of the track matching efficiency from the ITS to the TPC and the inverse momentum resolution for a 4-GEM stack as a function of several collisions. The efficiency and resolution only start to diminish at an event rate above 100 kHz, which is double the expected rate after the LHC upgrade, and are well within the range of the current TPC operating at 3.5 kHz.

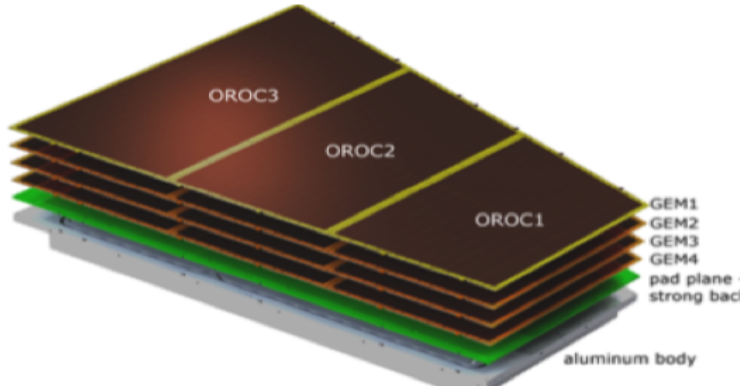


**Figure 4.5:** Final design of the upgraded readout chambers with a stack of 4 GEMS [16].

The optimal hole configuration was also explored with simulations. Having a first and forth layer with a pitch of  $140 \mu m$  and the second and third layer with a pitch of  $280 \mu m$ , allowed for the the ROCs to maintain minimal ion backflow while amplifying the signal from

tracks. Figure 4.5 shows the design of the ROCs with a 4-GEM stack. The copper pad plane is glued to a reinforced fiberglass sheet, known as the strongback, to add material strength.

## 2014 Test Beam

During the 2014 test beam, I mounted the prototypes on the beam line, recorded data from the test beam, and monitored the performance in real time. To quantify the performances of the prototype, it is useful to define the effective gain ( $G_{eff}$ ) and ionic backflow (IBF%)

$$G_{eff} = \frac{I_{anode}}{e N_{ion} R} \quad (4.1)$$

where  $e$  is the fundamental electric charge of an electron,  $N_{ion}$  is the number of captured ions, and  $R$  is the illumination rate from an active source.

$$IBF\% = \frac{I_{cathode}}{I_{anode}} = \frac{1 + \epsilon}{G_{eff}} \quad (4.2)$$

where  $I_{cathode}/I_{anode}$  is the ratio of the currents measured in the cathode and anode portion of a readout as seen in Figure 3.6. The IBF% can also be defined in terms of the number of backflowing ions ( $\epsilon$ ) created at an effective gain ( $G_{eff}$ ). The effective gain is a measure of the amplification properties and in a gaseous detector is defined as

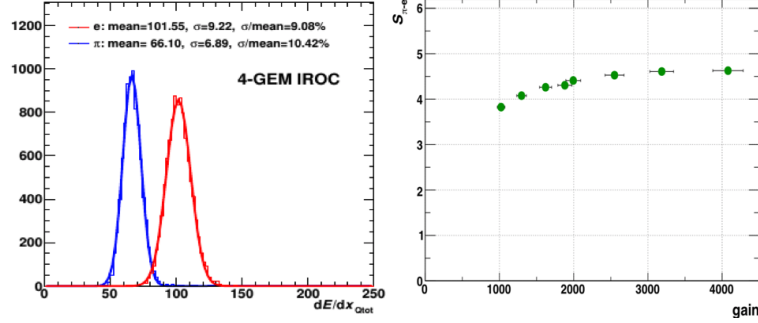
The test involved using the beam from both the SPS and PS<sup>2</sup> at the LHC cast onto an iron target. This iron target created secondary showers and tracks were measured by the prototype for both energy resolution and PID performance. The nominal TPC gas of  $CO_2 - N_2$  (90-10) was used during the test beam.

Figure 4.6 shows the PID performance for separating electron and pion tracks created by the iron target. The separation power between the two Gaussian peaks increases until a gain of 2000 so this was chosen as the target effective gain for the new ROCs.

Figure 4.7 shows the energy resolution of the iron peak as a function of the relative voltages between GEM 2 ( $U_{GEM2}$ ) and the ratio of voltages between GEM 3 ( $U_{GEM3}$ ) and GEM 4 ( $U_{GEM4}$ ). This shows that the IBF% remains below 1% at a energy resolution of approximately 10% which is consistent with the current TPC performance. The voltages

---

<sup>2</sup>See Section 3.1.2.



**Figure 4.6:**  $dE/dx$  resolution of the 4-GEM IROC prototype (*left*) and the separation power between electrons and pions as a function of gain (*right*) [17].

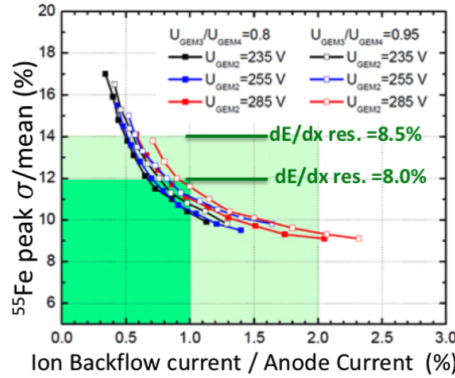


**Figure 4.7:** Energy resolution of the iron peak as measured from the prototype IROC with varying GEM voltages as a function of IBF% [17].

were chosen such that GEM 1 and GEM2, which are closest to the drift volume, would focus mostly on capturing amplification ions while GEM 3 and GEM 4, which are closest to the copper pad readout, would primarily perform the amplification as shown in Figure 4.8.

#### 4.0.4 Production of the Inner Readout Chambers in the U.S.

Once a final design was settled on from the simulation and prototype R&D, the project entered the production phase. A minimum of 36 new ROCs would need to be built with the 4-GEM stack to replace the old ROCs in the TPC while 4 additional ROCs would be constructed as spares. Due to the size and weight of the ROCs, production of the IROCs would take place in the United States and the OROC production mainly in Germany.

Figure 4.13 shows the production flow for the construction of the 4-GEM ROCs. After GEMs are received from the manufacturer, they go through a number of quality assurance tests

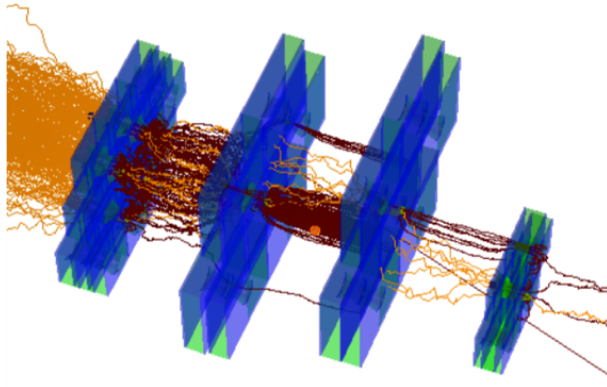


**Figure 4.8:** Simulation of the four GEM (blue) layers after test beam. The configuration is such that the two GEMs closest to the drift volume, right side, absorb the amplification ions created by the two GEMs closest to the readout (right) [17].

before they are shipped to Wayne State University, where they are stretched and mounted for the IROCs. The aluminum bodies are manufactured at the University of Texas Austin and shipped to Tennessee. At Tennessee we glue the pad plane, aluminum body and strong back together before it is shipped to Yale, where the chambers are fit with the GEMs from Wayne State. The production steps for the OROC mirror those performed by the IROC except that it was performed mainly German institutes.

Figure 4.10 shows the procedure followed at Tennessee in order to build an IROC. Furthest on the left is a picture of a copper pipe glued into the aluminum body. This copper pipe is flushed with a coolant that maintains the temperature of the Front End Electronics (FEE). The next two photos show the pad plane being mounted on a vacuum table while glue is applied to it and the aluminum body. Once all the components are placed glued and mounted on the table the IROC is loaded with lead bricks and allowed to cure for 24 hours. The right most picture shows the final step of the HV feedthroughs mounted and glued for the GEM foils. Before a completed IROC leaves Tennessee we performed a gas tightness test that will be discussed more in the next section. Full production of the IROCs ended in November of 2018 with a total of 47 chambers being built at Tennessee. A surplus of chambers were built with excess materials to provide spares.

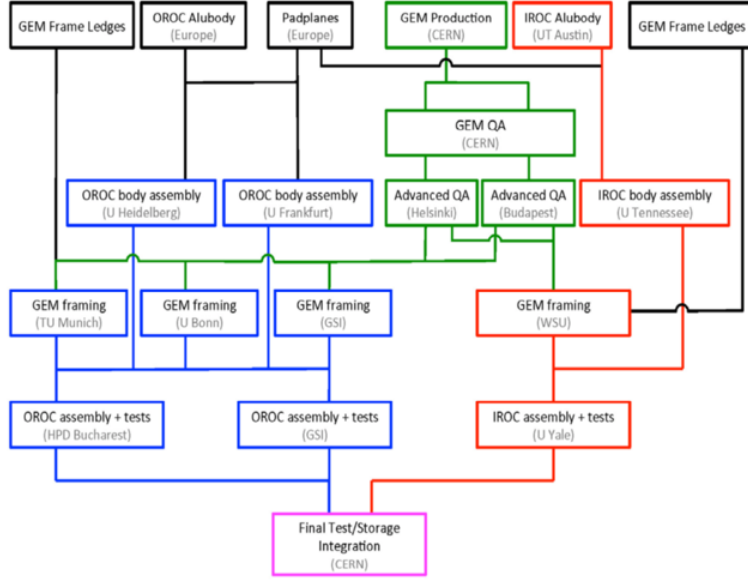


**Figure 4.9:** Production flow of the IROCs (red), OROCs (blue), and GEM foils (green)[15].



**Figure 4.10:** The author assembling an Inner Readout Chamber at the University of Tennessee.

#### 4.0.5 GEM and Chamber Quality Assurance

A stringent set of quality assurance (QA)[18][13] protocols were implemented to monitor any damage sustained during transport and to quickly identify any flaws in the production procedures. The QA can be broken into two major categories: QA performed on the GEM foils as received from the manufacturer and QA performed on complete/semi-complete

chambers as they were going through the different production steps. I will discuss only the QA tasks that I was directly involved with.

## GEM QA

In order to evaluate the performance of a GEM foil, a spark test was performed on every foil. Sparks are caused by the discharge of the foil and may be due to the presence of dust on a foil, imperfections in the hole geometry, or a short between the two copper layers of the GEM. The final design of the GEM foils had each foil segmented into twelve sectors with a  $10 M\Omega$  bias resistor across every segment. Any sparks that occur on the GEM will only discharge a given segment and not the entire foil. Because of the delicate nature of the GEM foil, sparks have the potential to permanently damage a foil or seriously affect the performance of a ROC. Thus GEMs with a high spark rate should be excluded as soon as possible in the production flow.

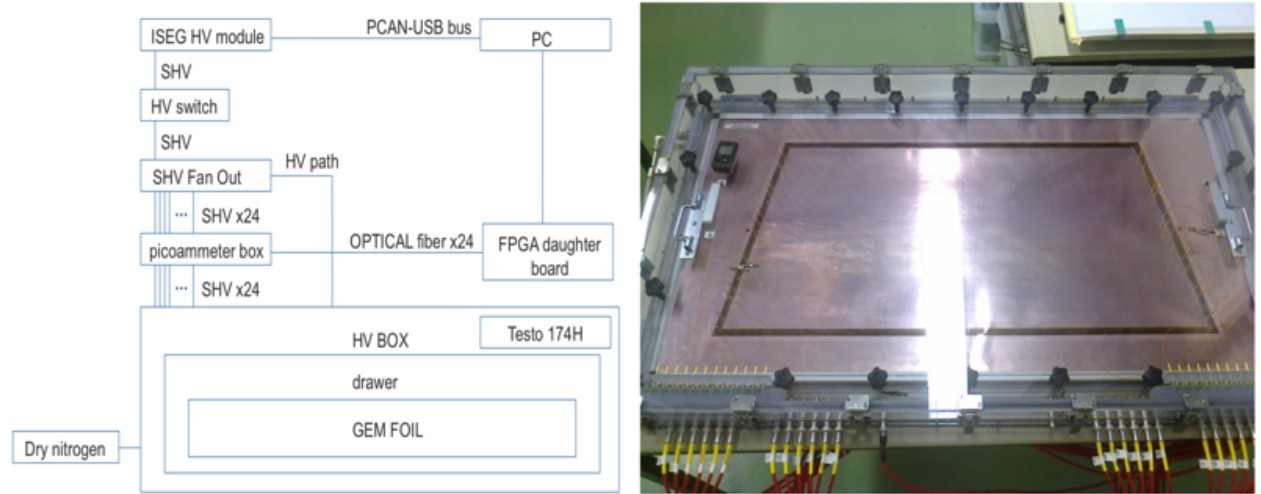


**Figure 4.11:** Schematic for the setup of the GEM foil spark test (*left*)<sup>[18]</sup> and the GEM mounted in the HV gas box (*right*).

The GEM foil spark test involves mounting each foil in a High Voltage (HV) box, which is flushed with  $N_2$  until it reaches a relative humidity of  $\approx 10\%$ . Once this humidity is reached 500 V is placed across each segment of the GEM and monitored with a LabView interface. A spark is defined as the LabView recording a current above 10 nA across the bias resistor through any GEM segment and read by a multi-channel picoammeter. The criteria for a GEM to fail this QA was to have more than five sparks over a 20 minute recording window.

## Chamber QA

Most of the QA I helped with was on ROC chambers as they went through the production steps. Before completed IROC chambers were sent to Yale, I performed a gas leak test. The leak test consisted of mounting an individual chamber into an aluminum test vessel and flushing the inside of the vessel with  $N_2$  gas. By using a flowmeter to measure the rate that  $N_2$  gas enters the test vessel and an oxygen sensor to measure the amount of oxygen present at the output of the test vessel we can infer the leak rate of each IROC chamber. Figure 4.12 shows a schematic of the setup (left) and what the typical output from the LabView interface (right). By flowing at two different rates and measuring the oxygen content at each rate we could confirm the leak rate.

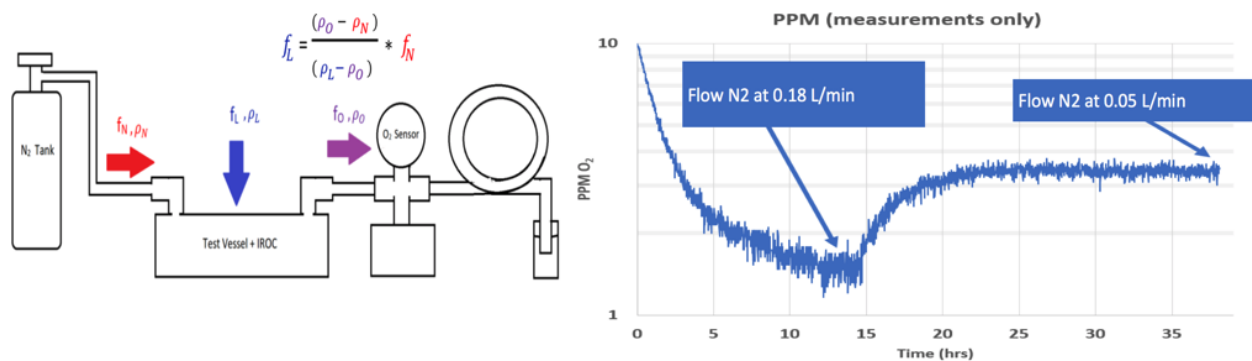


**Figure 4.12:** Schematic of the gas tightness testing setup at the University of Tennessee (*Courtesy of Joseph Rasson*).

The leak rate of a chamber,  $f_L$ , can be quantified as

$$f_L = \left( \frac{\rho_0 - \rho_N}{\rho_L - \rho_0} \right) f_N \quad (4.3)$$

where  $f_N$  is the flow rate of  $N_2$  gas into the test vessel,  $\rho_L$  is the concentration of  $O_2$  in the laboratory,  $\rho_N$  is the  $O_2$  impurity present in the  $N_2$  bottle, and  $\rho_0$  is the  $O_2$  reading from the LabView interface.

A maximum leak rate of 0.25 mL/hour was placed as the rejection criteria for a given chamber. If a chamber had a leak rate above this the  $N_2$  gas could get swapped out with a helium gas tank and we could use a helium sniffer to identify the areas on the IROC

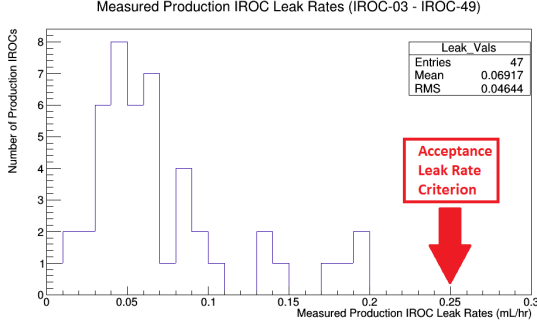


**Figure 4.13:** Leak rate of the 47 chambers built at Tennessee with the maximum failure rate at 0.25 ml/hr shown (*Courtesy of Charles Hughes*).

causing the leak and patch the area with epoxy. Figure 4.13 shows the leak rate for all IROCs produced at Tennessee, due to none of the chambers surpassing the leak threshold the helium sniffer was not used in the production of the IROCs.

Once an IROC chamber was fitted with the 4 GEM foils at Yale and sent to CERN a spark test was performed over the entire chamber. The test involved placing each chamber next to the LHC beam line, flushing with the nominal TPC gas, and placing the nominal voltage across each GEM and monitoring the spark rate once a beam was present in the LHC. Figure 4.14 shows myself installing the completed IROC chambers next to the LHC beam line in front of ALICE and the output from the spark monitor. The voltage across each chamber could be varied in real time in order to minimize sparking while maintaining the IROC performance, thus reducing the rate of degradation on a per chamber basis once installed in the TPC.

#### 4.0.6 Outlook

As of November 2018, the 47 IROCs assembled at Tennessee have been received at CERN. None of the built chambers have surpassed the gas leak test performed at CERN and so far only 4 chambers exhibit sparking rates above the threshold. By May of 2019, the LHC beamline around ALICE will be decommissioned and the TPC will be moved to a surface level clean room for the installation of the chambers. The installation of the new FEE electronics and the ROC chambers should take place throughout the summer of 2019. Afterwards there will be a 10 month commissioning with the TPC, during which the performance of the

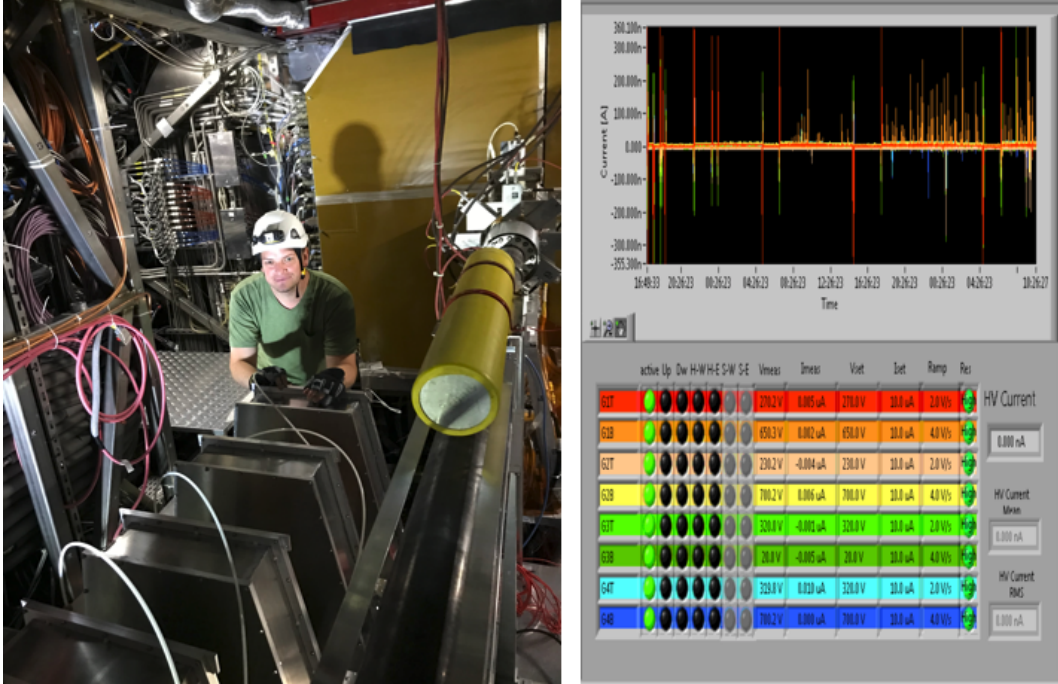


**Figure 4.14:** The author testing spark testing chambers next to the LHC beam line (*left*) and real time output from the spark test during a live beam (*right*).

upgraded TPC will be evaluated with cosmic rays. By the end of 2020, the TPC should be back in the ALICE cavern and the beam line will have been re-installed. The Hi-Lumi run of the LHC is expected to start in March of 2021.

# Chapter 5

## Jet Results and Discussion

Beginning in March of 2012, the LHC began seven months of pp collisions at  $\sqrt{s} = 8$  TeV. The jet cross sections and ratios of the cross sections for jets of different radii offers a unique perspective on the pQCD effects of hadronization at this new energy frontier. Due to the expectation that no QGP is formed in a pp collision these measurements serve as a baseline for separating phenomena associated with the QGP in heavy-ion collisions. In order to measure the jet cross section the following formula is used,

$$\frac{d\sigma^{jet}}{d\eta dp_T} = \frac{A_{trigger}}{\epsilon_{trigger}(p_T)} \times C_{MC} \times \frac{1}{A(p_T)} \times \frac{1}{L_{int}} \times \frac{dN^{jet}}{dp_T d\eta} \quad (5.1)$$

where,

- $A_{trigger}$  is the acceptance for EMCal triggered events and  $\epsilon_{trigger}(p_T)$  is the EMCal trigger efficiency. These factors correct for imperfections in the electronics of the EMCal and the overall factors are equal to one in minimum bias events.
- $C_{MC}$  is a correction factor due to detector effects and it allows for comparisons between the ALICE experiment to other experiments or theoretical calculations. Unfolding is used to determine this factor.
- $L_{int}$  is the integrated luminosity during the period when the data was recorded.
- $A(p_T)$  is the geometrical detector acceptance.

- $\frac{dN^{jet}}{dp_T d\eta}$  is the inclusive jet momentum spectra.

The following sections will go over how each factor was determined and the quality assurance procedures used for this analysis.

## 5.1 Data Quality

ALICE is a state-of-the-art experiment with excellent tracking and particle identification capabilities as discussed in Chapter 3. However, just like any real world experiment, it contains a number of inefficiencies and imperfections. This means that the data collected during the 8 TeV pp collision must be examined and any inaccuracies in the data must be removed before hard physics conclusions may be reached. Data may be compromised at both the event-level, the experiment erroneously recorded something as an event, or at the constituent-level, one of the subdetectors mismeasured a feature of a particle, and these outliers must be accounted for and removed

## 5.2 Event Selection

During the 8 TeV data collection period approximately 180 million minimum bias events were recorded, as summarized in table ?? . These events are separated into periods, which dictate the particular beam and detector configurations during the data taking. The 8 TeV data is broken into 7 periods with approximately 181 million minimum bias events recorded.

Period	# of runs	# of Min Bias events
LHC12c	89	$\sim 24$ M
LHC12d	140	$\sim 62$ M
LHC12e	5	$\sim 2$ M
LHC12f	56	$\sim 15$ M
LHC12g	8	$\sim 0.4$ M
LHC12h	159	$\sim 75$ M
LHC12i	40	$\sim 3$ M
Total	497	$\sim 181$ M

**Table 5.1:** 2012 8 TeV data taking period.

Approximately, 15% of the data sampled is unusable due to malfunctions in TPC chambers, EMCal super modules, the electronics for the EMCal or TPC, and

### 5.3 Raw measurements

The ALICE experiment is capable of two types of jet reconstruction, charged and full jets. Charged jets use information from the charged particle tracking detectors, such as the ITS and TPC, in conjunction with a jet finding algorithm to identify jets. Full jets implement a similar procedure but also incorporates the EMCal in order to

### 5.3.1 Raw Jet Momentum Spectra in pp Collisions

## 5.4 Unfolding

### 5.4.1 Corrections to particle Level

### 5.4.2 Unfolding Matrix

### 5.4.3 Unfolded Spectra

## 5.5 Trigger Efficiency

## 5.6 Systematic Uncertainties

### 5.6.1 Systematic Uncertainty to Jet Yield

### 5.6.2 Systematic Uncertainty to Jet Energy Scale

### 5.6.3 Total Uncertainty

## 5.7 Corrected pp jet cross section

### 5.7.1 Comparisons to pQCD predictions

### 5.7.2 Jet Cross Section and Ratios

Given two jets of different radii,  $R_1$  and  $R_2$ , the ratio of the cross sections may be written in short hand as,

$$\frac{\sigma_{R_1}}{\sigma_{R_2}} = \frac{d\sigma_{R_1}^{jet}}{d\eta dp_T} / \frac{d\sigma_{R_2}^{jet}}{d\eta dp_T} \quad (5.2)$$

# **Chapter 6**

## **Conclusion and Outlook**

# Bibliography

- [1] C. Patrignani et al. Review of Particle Physics. *Chin. Phys.*, C40(10):100001, 2016. [vi](#), [viii](#), [1](#), [50](#)
- [2] Vardan Khachatryan et al. Measurement of the inclusive 3-jet production differential cross section in proton–proton collisions at 7 TeV and determination of the strong coupling constant in the TeV range. *Eur. Phys. J.*, C75(5):186, 2015. [vi](#), [5](#)
- [3] Esma Mobs. The CERN accelerator complex. Complexe des accélérateurs du CERN. Jul 2016. General Photo. [vi](#), [11](#)
- [4] W. M. Alberico, A. Beraudo, A. De Pace, A. Molinari, M. Monteno, M. Nardi, and F. Prino. Heavy-flavour spectra in high energy nucleus-nucleus collisions. *Eur. Phys. J.*, C71:1666, 2011. [vi](#), [13](#)
- [5] Jaroslav Adam et al. Centrality dependence of the charged-particle multiplicity density at midrapidity in Pb-Pb collisions at  $\sqrt{s_{\text{NN}}} = 5.02$  TeV. *Phys. Rev. Lett.*, 116(22):222302, 2016. [vi](#), [15](#)
- [6] J. Alme et al. The ALICE TPC, a large 3-dimensional tracking device with fast readout for ultra-high multiplicity events. *Nuclear Instruments and Methods in Physics Research A*, 622:316–367, October 2010. [vi](#), [16](#)
- [7] Ralf Diener. Gas amplification with micro pattern gas detectors. [vi](#), [17](#)
- [8] Betty Bezverkhny Abelev et al. Performance of the ALICE Experiment at the CERN LHC. *Int. J. Mod. Phys.*, A29:1430044, 2014. [vi](#), [18](#)
- [9] G Bourdaud. Gamma-jet physics with the electro-magnetic calorimeter in the alice experiment at lhc. *Journal of Physics: Conference Series*, 110(3):032006, 2008. [vi](#), [19](#)
- [10] U. Abeysekara et al. ALICE EMCal Physics Performance Report. 2010. [vi](#), [21](#)
- [11] Cristiane Jahnke.  $J/\psi$  production as a function of event multiplicity in pp collisions at  $\sqrt{s} = 13$  TeV using EMCAL-triggered events with ALICE at the LHC. In *14th International Workshop on Hadron Physics (Hadron Physics 2018) Florianopolis, Santa Catarina, Brazil, March 18-23, 2018*, 2018. [vi](#), [22](#)

- [12] B Abelev et al. Upgrade of the ALICE Experiment: Letter of Intent. Technical Report CERN-LHCC-2012-012. LHCC-I-022. ALICE-UG-002, CERN, Geneva, Aug 2012. [vii](#), [24](#), [25](#)
- [13] Erik Brücke and Timo Hildén. GEM Foil Quality Assurance For The ALICE TPC Upgrade. *EPJ Web Conf.*, 174:03004, 2018. [vii](#), [26](#), [32](#)
- [14] Purba Bhattacharya, Bedangadas Mohanty, Supratik Mukhopadhyay, Nayana Majumdar, and Hugo Natal da Luz. 3D simulation of electron and ion transmission of GEM-based detectors. *Nucl. Instrum. Meth.*, A870:64–72, 2017. [vii](#), [27](#)
- [15] Dick Majka. The alice tpc upgrade project. *Quark Matter 2017*, 2017. [vii](#), [28](#), [32](#)
- [16] Upgrade of the ALICE Time Projection Chamber. Technical Report CERN-LHCC-2013-020. ALICE-TDR-016, Oct 2013. [vii](#), [25](#), [28](#)
- [17] Addendum to the Technical Design Report for the Upgrade of the ALICE Time Projection Chamber. Technical Report CERN-LHCC-2015-002. ALICE-TDR-016-ADD-1, Feb 2015. [vii](#), [25](#), [30](#), [31](#)
- [18] Jens Erik Brücke and Timo Eero Hildén. The GEM QA Protocol of the ALICE TPC Upgrade Project. In *5th International Conference on Micro Pattern Gas Detectors (MPGD2017) Temple University, Philadelphia, USA, May 22-26, 2017*, 2018. [vii](#), [32](#), [33](#)
- [19] Francesco Noferini. The ALICE PID performance in Run 1 and perspectives in view of Run 2. In *Proceedings, 3rd Large Hadron Collider Physics Conference (LHC 2015): St. Petersburg, Russia, August 31-September 5, 2015*, pages 523–528, Gatchina, 2016. Kurchatov Institute, Kurchatov Institute. [viii](#), [51](#)
- [20] Paul Langacker. Introduction to the Standard Model and Electroweak Physics. In *Proceedings of Theoretical Advanced Study Institute in Elementary Particle Physics on The dawn of the LHC era (TASI 2008): Boulder, USA, June 2-27, 2008*, pages 3–48, 2010. [1](#)

- [21] Tatsumi Aoyama, M. Hayakawa, Toichiro Kinoshita, and Makiko Nio. Tenth-Order Electron Anomalous Magnetic Moment — Contribution of Diagrams without Closed Lepton Loops. *Phys. Rev.*, D91(3):033006, 2015. [Erratum: Phys. Rev.D96,no.1,019901(2017)]. [2](#)
- [22] Michael Riordan. The discovery of quarks. *Science*, 256(5061):1287–1293, 1992. [4](#)
- [23] Frank Wilczek. Asymptotic freedom: From paradox to paradigm. *Proc. Nat. Acad. Sci.*, 102:8403–8413, 2005. [Rev. Mod. Phys.77,857(2005)]. [5](#)
- [24] Constantin Loizides. Glauber modeling of high-energy nuclear collisions at the subnucleon level. *Phys. Rev.*, C94(2):024914, 2016. [7](#), [16](#)
- [25] Michael L. Miller, Klaus Reygers, Stephen J. Sanders, and Peter Steinberg. Glauber modeling in high energy nuclear collisions. *Ann. Rev. Nucl. Part. Sci.*, 57:205–243, 2007. [7](#)
- [26] J E Huth, N Wainer, K Meier, N J Hadley, F Aversa, Mario Greco, P Chiappetta, J P Guillet, S Ellis, Zoltán Kunszt, and Davison Eugene Soper. Toward a standardization of jet definitions. (FERMILAB-CONF-90-249-E):7 p, Dec 1990. [8](#)
- [27] STEPHEN MYERS. The large hadron collider 2008–2013. *International Journal of Modern Physics A*, 28(25):1330035, 2013. [10](#)
- [28] Thomas Taylor and Daniel Treille. The Large Electron Positron Collider (LEP): Probing the Standard Model. *Adv. Ser. Direct. High Energy Phys.*, 27:217–261, 2017. [10](#)
- [29] G. Aad et al. The ATLAS Experiment at the CERN Large Hadron Collider. *JINST*, 3:S08003, 2008. [10](#)
- [30] S. Chatrchyan et al. The CMS Experiment at the CERN LHC. *JINST*, 3:S08004, 2008. [10](#)
- [31] A. Augusto Alves, Jr. et al. The LHCb Detector at the LHC. *JINST*, 3:S08005, 2008. [10](#)

- [32] K. Aamodt et al. The ALICE experiment at the CERN LHC. *JINST*, 3:S08002, 2008. [10](#)
- [33] Serguei Chatrchyan et al. Observation of a new boson at a mass of 125 GeV with the CMS experiment at the LHC. *Phys. Lett.*, B716:30–61, 2012. [10](#)
- [34] Georges Aad et al. Observation of a new particle in the search for the Standard Model Higgs boson with the ATLAS detector at the LHC. *Phys. Lett.*, B716:1–29, 2012. [10](#)
- [35] C. Fabjan and J. Schukraft. The Story of ALICE: Building the dedicated heavy ion detector at LHC. In '*The Large Hadron Collider: A marvel technology*', EPFL-Press Lausanne, Switzerland, 2009 (Editor: L. Evans), chapter 5.4, 2011. [12](#), [13](#)
- [36] Vladimir V. Gligorov, Simon Knapen, Benjamin Nachman, Michele Papucci, and Dean J. Robinson. Leveraging the ALICE/L3 cavern for long-lived exotics. 2018. [14](#)
- [37] M. Bondila et al. ALICE T0 detector. *IEEE Trans. Nucl. Sci.*, 52:1705–1711, 2005. [14](#)
- [38] E. Abbas et al. Performance of the ALICE VZERO system. *JINST*, 8:P10016, 2013. [14](#)
- [39] Rick Field. Min-Bias and the Underlying Event at the LHC. *Acta Phys. Polon.*, B42:2631–2656, 2011. [14](#)
- [40] S. Beolè. The alice inner tracking system: Performance with proton and lead beams. *Physics Procedia*, 37:1062 – 1069, 2012. Proceedings of the 2nd International Conference on Technology and Instrumentation in Particle Physics (TIPP 2011). [15](#)
- [41] Jaroslav Adam et al. Particle identification in ALICE: a Bayesian approach. *Eur. Phys. J. Plus*, 131(5):168, 2016. [15](#)
- [42] Christian Lippmann. Performance of the alice time projection chamber. *Physics Procedia*, 37:434 – 441, 2012. Proceedings of the 2nd International Conference on Technology and Instrumentation in Particle Physics (TIPP 2011). [18](#)
- [43] A Fantoni and the ALICE collaboration. The alice electromagnetic calorimeter: Emcal. *Journal of Physics: Conference Series*, 293(1):012043, 2011. [19](#)

- [44] Olivier Bourrion, R Guernane, B Boyer, JL Bouly, and G Marcotte. Level-1 jet trigger hardware for the alice electromagnetic calorimeter at lhc. *Journal of Instrumentation*, 5(12):C12048, 2010. [21](#)
- [45] O Bourrion, N Arbor, G Conesa-Balbastre, C Furget, R Guernane, and G Marcotte. The alice emcal l1 trigger first year of operation experience. *Journal of Instrumentation*, 8(01):C01013, 2013. [21](#)
- [46] Jiri Kral, Terry Awes, Hans Muller, Jan Rak, and Joachim Schambach. {L0} trigger for the {EMCal} detector of the {ALICE} experiment. *Nuclear Instruments and Methods in Physics Research Section A: Accelerators, Spectrometers, Detectors and Associated Equipment*, 693:261 – 267, 2012. [21](#)
- [47] G Apollinari, I Béjar Alonso, O Brüning, M Lamont, and L Rossi. High-Luminosity Large Hadron Collider (HL-LHC) : Preliminary Design Report. 2015. [23](#)
- [48] Levente Molnar and the ALICE Collaboration. Upgrade and physics perspective of alice at the lhc. *Journal of Physics: Conference Series*, 589(1):012014, 2015. [24](#)
- [49] T L Karavicheva and ALICE Collaboration. The fast interaction trigger detector for the alice upgrade. *Journal of Physics: Conference Series*, 798(1):012186, 2017. [24](#)
- [50] B Abelev and all. Technical Design Report for the Upgrade of the ALICE Inner Tracking System. Technical Report CERN-LHCC-2013-024. ALICE-TDR-017, Nov 2013. [24](#)
- [51] Technical Design Report for the Muon Forward Tracker. Technical Report CERN-LHCC-2015-001. ALICE-TDR-018, Jan 2015. [24](#)
- [52] P Buncic, M Krzewicki, and P Vande Vyvre. Technical Design Report for the Upgrade of the Online-Offline Computing System. Technical Report CERN-LHCC-2015-006. ALICE-TDR-019, Apr 2015. [24](#)
- [53] Radoslaw Ryblewski and Michael Strickland. Dilepton production from the quark-gluon plasma using leading-order (3+1)D anisotropic hydrodynamics. *Acta Phys. Polon. Supp.*, 8(2):445, 2015. [24](#)

- [54] Mauricio Martinez and Michael Strickland. Measuring QGP thermalization time with dileptons. *Phys. Rev. Lett.*, 100:102301, 2008. [24](#)
- [55] F. Sauli. GEM: A new concept for electron amplification in gas detectors. *Nucl. Instrum. Meth.*, A386:531–534, 1997. [25](#)
- [56] Maxim Titov. Perspectives of Micro-Pattern Gaseous Detector Technologies for Future Physics Projects. In *Proceedings, CMS Workshop: Perspectives on Physics and on CMS at Very High Luminosity, HL-LHC: Alushta, Crimea, Ukraine, May 28–31, 2012*, pages 241–258, 2013. [26](#)
- [57] M Tang, A Q Liu, A Agarwal, and M H Habib. A single-mask substrate transfer technique for the fabrication of high-aspect-ratio micromachined structures. *Journal of Micromechanics and Microengineering*, 17(8):1575, 2007. [27](#)
- [58] W. You, Y. Zhou, J. Liu, M. Shao, C. Li, H. Chen, Z. Tang, Y. Sun, Y. Zhang, Y. Lv, G. Song, X. Wang, D. Hu, and D. Hong. A new technique for assembling large-size gem detectors. *Journal of Instrumentation*, 12(06):C06036, 2017. [27](#)
- [59] Fabio Sauli. The gas electron multiplier (gem): Operating principles and applications. *Nuclear Instruments and Methods in Physics Research Section A: Accelerators, Spectrometers, Detectors and Associated Equipment*, 805:2 – 24, 2016. Special Issue in memory of Glenn F. Knoll. [27](#)
- [60] Marco Santimaria and Davide Pinci. Study of the GEM detector for the LHCb experiment upgrade, Nov 2013. Presented 19 Dec 2013. [27](#)
- [61] S. Agostinelli et al. GEANT4: A Simulation toolkit. *Nucl. Instrum. Meth.*, A506:250–303, 2003. [27](#)
- [62] Betty Bezverkhny Abelev et al. Production of charged pions, kaons and protons at large transverse momenta in pp and Pb–Pb collisions at  $\sqrt{s_{\text{NN}}} = 2.76$  TeV. *Phys. Lett.*, B736:196–207, 2014. [51](#)

# Appendices

## A Particle Identification via Bethe-Bloch

The energy loss of a relativistic charged particle traversing through a medium is given by the Bethe-Bloch relation:

$$\frac{dE}{dx} \propto \frac{1}{\beta^2} \frac{Z}{A} \rho \left[ \frac{1}{2} \ln \frac{2m_e c^2 \beta^2 \gamma^2 T_{max}}{I^2} - \beta^2 - \frac{\delta(\beta\gamma)}{2} \right] \quad (1)$$

where  $\rho$  is the density of the medium,  $\frac{Z}{A}$  is the ratio of the atomic number to the atomic mass of the absorber,  $\beta$  is the ratio of the particle's momentum to energy,  $T_{max}$  is the maximum transfer energy from the charged particle to an electron in the medium,  $I^2$  is the mean excitation energy of the medium,  $\frac{\delta(\beta\gamma)}{2}$  is a correction factor based on the polarization of the material, and  $\gamma^2$  is the lorentz factor  $\frac{1}{\sqrt{1-\beta^2}}$

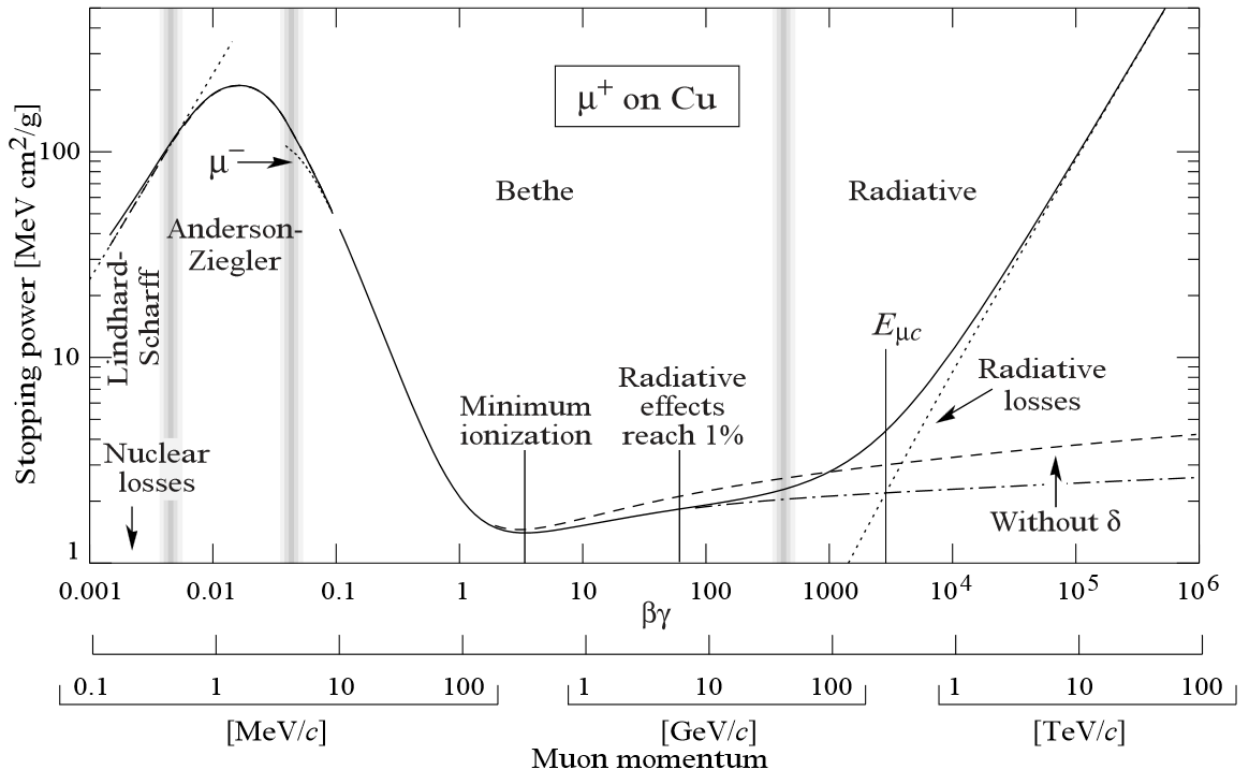


**Figure 1:** Energy loss of a muon traversing a copper medium between 0.1 MeV to 100 TeV [1].

Figure 1 shows the Bethe-Bloch curve for a muon over a wide kinematic range. At low energies the dominate form of energy loss is via elastic scattering, while at high energies

radiation becomes the dominate energy loss mechanism. When  $\beta\gamma \approx 3$  the muon losses the least amount of energy possible and is called a minimum ionization particle(MIP).

The ALICE ITS and TPC<sup>1</sup> cannot directly measure the energy loss of a particle traversing either sub-detector. Instead they perform PID by measuring the relative amplitudes from the sub-detectors read-out elements, pixels in the ITS and copper pads in the TPC. The amplitudes are then fit to the Bethe-Bloch equation as seen in Figure 2. Electrons weakly obey the Bethe-Bloch relationship in the kinematic ranges sensitive to the ITS and TPC and thus have a constant energy loss in both detectors.

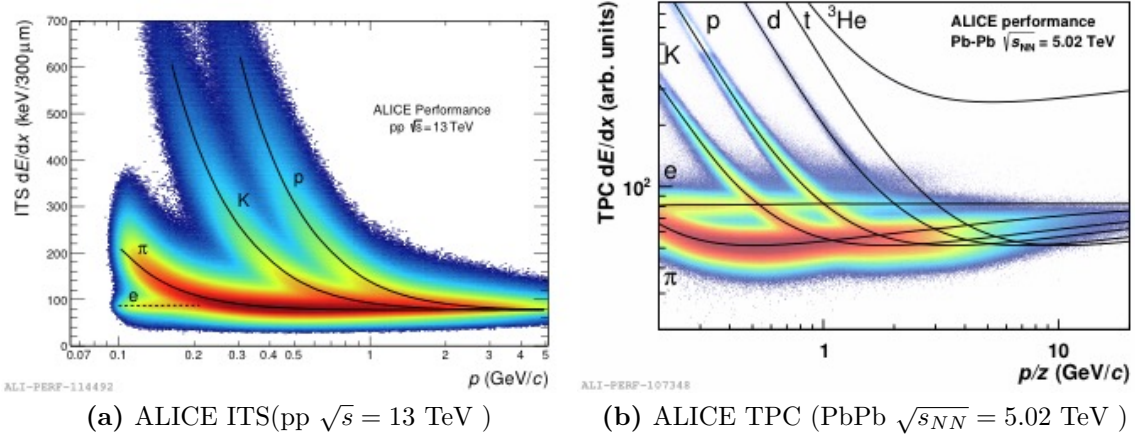


**Figure 2:** Specific energy loss for the ITS(*left*) and the TPC(*right*) with Bethe-Bloch fits from different particle species traversing each detector[19].

Figure 2 also shows that the Bethe-Bloch curves merge above some kinematic range, 4 GeV in the ITS and 10 GeV in the TPC. Above this kinematic range particles cannot be distinguished on a track-by-track basis, but by using statistical methods and Gaussian fits PID can be extended up to 20 GeV[62].

---

<sup>1</sup>See Section 3.2.3 and Section 3.2.4

# Vita